

CHAPTER II

LITERATURE REVIEW

2.1 Thermoelectricity

2.1.1 Introduction

Thermoelectric technology, a renewable energy, has been used to directly convert heat into electricity current since 19th century. The first discovery of the thermal effect was found by Thomas Johann Seebeck in 1821. This phenomenon exposed that an electromotive current could be generated by heating a junction between different metals, this phenomenon is known as “Seebeck effect” (Goldsmid, 2010). A few years later, Jean Charles Athanase Peltier’s experiment demonstrated that heating and cooling could be induced by applying electrical current through metallic thermocouples. This phenomenon became known as the “Peltier effect” (Crawford, 2014). In 1855, W. Thomson (Lord Kelvin) described correlation between Seebeck effect and Peltier effect, which become known as “Kelvin relation” (applied with Onsager relation). Furthermore, W. Thomson also defined “Thomson effect” by applying thermodynamic theory to describe reversible heating and cooling along with the flow of electrical current and temperature gradient. Then, Edmund Altenkirch was the first one who derived the maximal efficiency of thermoelectric generator using constant properties of heat supply and output power per unit time. Edmund Altenkirch also provided the first correct calculation of thermoelectric power generator and defined concept of “figure of merit” which indicates that optimal thermoelectric materials should expressed a high Seebeck coefficient, high electrical conductivity and low thermal conductivity. Later in 1949, Abram Fedorovich Ioffe developed the modern dimensionless parameter of “figure of merit (ZT)” which approximates constant thermoelectric properties to indicating performance of thermoelectric materials (Saini *et al.*, 2021). Nowadays, thermoelectric properties have been developed in semiconductor materials (p-type and n-type), alloy materials, and oxide materials for use in electrical devices and industrials engines.

2.1.2 Theoretical background

As well known, Thomas Johann Seebeck was the first one who found

the phenomenon of electromotive current occurring at the junctions of two different conductor metals (A–B junctions). This phenomenon occurred when the junctions were subjected to a temperature difference, with one end being heated and the other cooled. The phenomena, known as “Seebeck effect” (Goldsmid, 2010). The Seebeck effect is illustrated in Figure 1. The mathematical parameters of the Seebeck effect relations describe temperature gradient across the junctions (A–B junctions) (ΔT or $T_H - T_C$), the potential difference between the end of the junctions (ΔV), and a parameter called “Seebeck coefficient” (α). The Seebeck effect relations is represented by the equation below.

$$\alpha = \frac{\Delta V}{\Delta T} \quad (1)$$

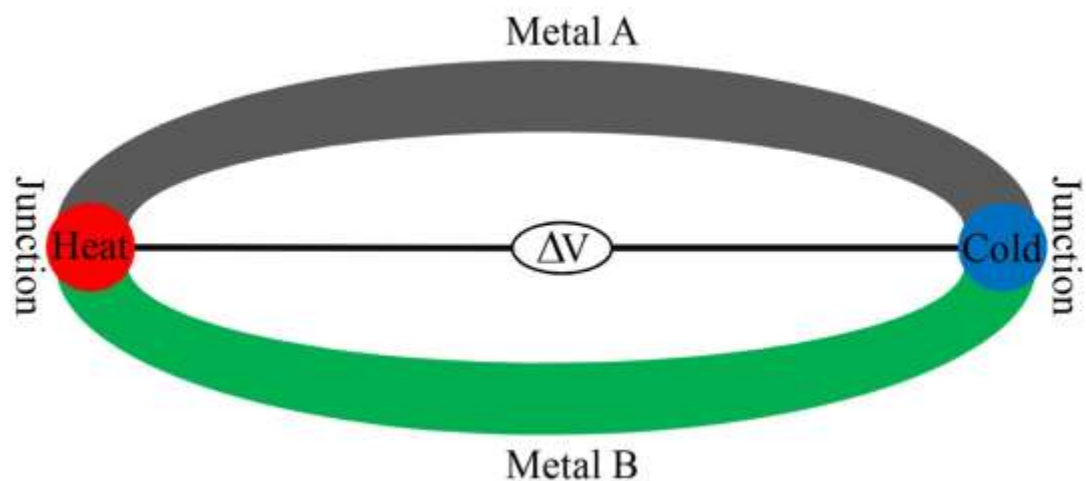


Figure 1 Illustration of Seebeck effect, adapted from Saini *et al.*, 2021 .

Jean Charles Athanase Peltier’s experiment demonstrated a slight change in temperature in a thermocouple when an electrical current was passed through it. The effect is associated with the heat transfer that occurs when electrical current was applied to the conductor metals junctions (A–B junctions), causing heating at one junction and cooling at the other. This phenomenon, known as the "Peltier effect," is illustrated in Figure 2. The mathematical parameters of Peltier effect relations describe release/absorption rate at the junctions (Q), electrical current supply (I) and a parameter named “Peltier coefficient” (Π). Peltier coefficient relations is represented by equation (2).

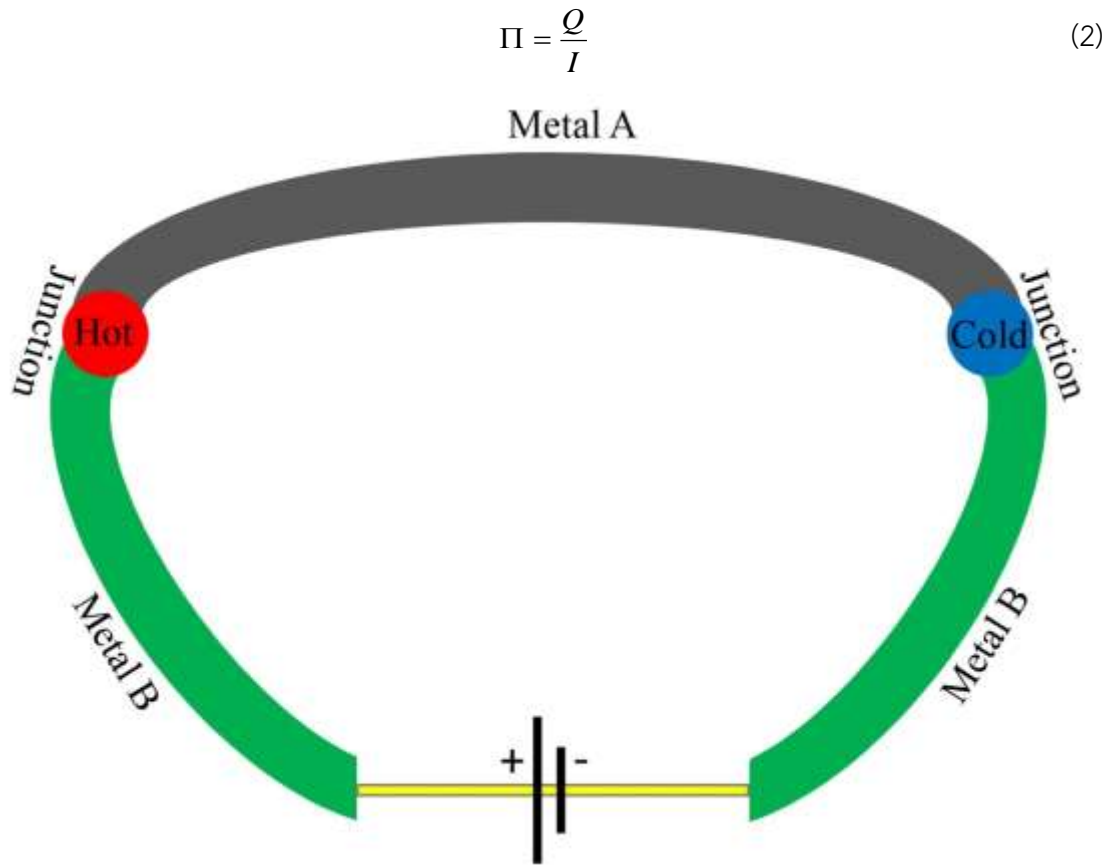


Figure 2 Illustration of Peltier effect, adapted from Saini *et al.*, 2021.

W. Thomson, also known as Lord Kelvin, established a connection between relation of the Seebeck coefficient and the Peltier coefficient using thermodynamic theory, a correlation known as the “Kelvin relation”, as shown in equation below.

$$\Pi = \alpha T \quad (3)$$

Moreover, W. Thomson defined the “Thomson effect”, which explains the rate of heat absorption and release in a conductor materials ($\dot{Q} = -\kappa \Delta^2 T$) as a function of temperature gradient (ΔT) and electrical current density (J). The Thomson effect is illustrated in Figure 3. The mathematical expression of Thomson effect is derived in the equation below (Saini *et al.*, 2021).

$$\dot{Q} = \frac{J^2}{\sigma} - J \left(\frac{T \partial \alpha}{\partial T} \right) \Delta T \quad (4)$$

Here, the term $\frac{T \partial \alpha}{\partial T}$ defined as “Thomson coefficient” μ . Consequently, the

Thomson coefficient can be derived as shown in equation (5).

$$\mu = \frac{T \partial \alpha}{\partial T} \quad (5)$$

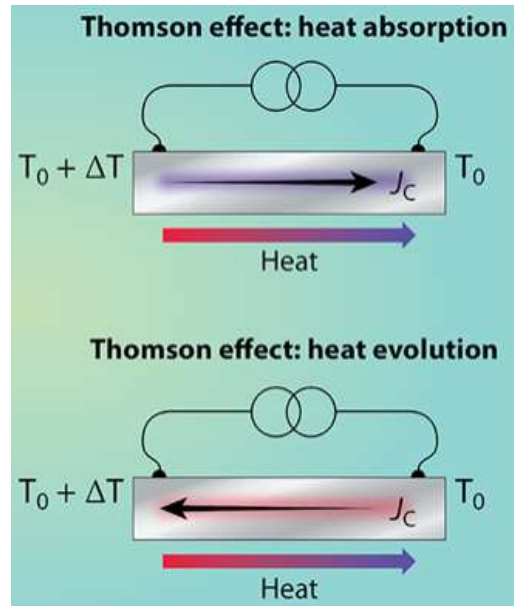


Figure 3 Illustration to demonstrate Thomson effect (Morrison and Dejene, 2020).

The key coupled transport equations of electrons and heat, based on thermodynamic theory, were derived using the Boltzmann transport equation, diffusion approximations, the Fermi–Dirac distribution, Ohm’s law, Fourier law, and Onsager’s reciprocal relations. This derivation process of the couple transport equations follows the methodology outlined in the book of “Nanoscale energy transport and conversion” by Gang Chen (Chen, 2005). The transport equation originates from the generalization of the continuity equation. When applied with the conservation of mass, this is referred to as “convection–diffusion equation” ($\frac{\partial c}{\partial t} + \nabla \cdot \mathbf{j} = \mathcal{S}$) such as Boltzmann transport equation. Then Boltzmann transport equation is used to describe changes in microscopy quantities, such as electrons and heat, within a thermodynamic system. The Boltzmann transport equation is shown in equation below (6) (Crawford, 2014).

$$\frac{\partial f}{\partial t} + \mathbf{v} \cdot \nabla_r f + \mathbf{F} \cdot \Delta_p f = \left. \frac{\partial f}{\partial t} \right|_{\text{collid}} + s(\mathbf{r}, \mathbf{p}, t) \quad (6)$$

Where;

f is a scalar quantity in the control volume.

$\frac{\partial f}{\partial t}$ is the time dependent variant term of quantity f in the control volume.

$\frac{\partial f}{\partial t} \Big|_{\text{collid}}$ is the time dependent collision term when f is a quantity of particles

$v \cdot \nabla_r f + F \cdot \Delta_p f$ is net balance quantity that enters or exits and the control volume.

r is real space.

p is momentum space.

F is force that influential in changing momentum space.

$s(r, p, t)$ is source term that represent amount of scalar quantity increase and decrease.

Due to the unidentified or absent source of the scalar quantity “ $s(r, p, t) = 0$ ” and the relaxation time approximation (τ , $\frac{1}{\tau} = \sum_i \frac{1}{\tau_i}$) is applied to obtain

$\frac{\partial f}{\partial t} \Big|_{\text{collid}} = \frac{f - f_0}{\tau}$, as shown in equation (7).

$$\frac{\partial f}{\partial t} + v \cdot \nabla_r f + F \cdot \Delta_p f = \frac{f - f_0}{\tau} \quad (7)$$

Where;

f_0 is a symmetric in momentum with average velocity is zero (Indeed, f_0 is a distribution function).

τ is the relaxation time approximation that is inverse of all scattering process of particles in the control volume as $\frac{1}{\tau} = \sum_i \frac{1}{\tau_i}$.

Then, the diffusion approximation is used to determine the appropriate distribution function for f . A deviation function g is defined by applying perturbation method for f . The function g is shown in equation (8).

$$g = f - f_0 \quad (8)$$

Then, substituted equation (8) in equation (7).

$$\frac{\partial f_0}{\partial t} + \frac{\partial g}{\partial t} + v \cdot \nabla_r f_0 + v \cdot \nabla_r g + F \cdot \Delta_p f_0 + F \cdot \Delta_p g = \frac{g}{\tau} \quad (9)$$

Due to the process stay in “steady state”, the variable f_0 is unchanged in time, $\frac{\partial g}{\partial t}$ and

$\nabla_r g$ too smaller than f and f_0 (diffusion law). Therefore, the equation (9) is changed.

$$g = \tau(v \cdot \nabla_r f_0 + F \cdot \Delta_p f_0) \quad (10)$$

Substituted equation (10) in equation (8).

$$f = f_0 + \tau(v \cdot \nabla_r f_0 + F \cdot \Delta_p f_0) \quad (11)$$

The distribution function of f can be extended using Fermi–Dirac distribution, which applied to fermions/particles with half–integer spin, including electrons. The Fermi–Dirac distribution is demonstrated equation (12).

$$f_0 = \frac{1}{e^{\frac{(E-E_f)}{k_B T}} + 1} \quad (12)$$

For electrons, the energy of state E is defined as $E = E_c + E_f$ where E_c is the conduction energy and E_f is Femi level energy (the absolute different energy above the conduction energy). Then, to define the force acting which interacted on the flow of electrons in the presence of an electric field, Ohm’s law and the Wiedemann–Franz law are applied.

$$F = -e\bar{E} \quad (13)$$

$$-e\bar{E} = e\nabla\Phi \quad (14)$$

Where;

F is force which interacted on electrons

e is electrons charge

\bar{E} is electric field ($\bar{E} = \frac{\partial V_{external}}{\partial r}$)

Φ is electrical potential

Then, the energy of electron conduction energy and Femi–level energy are derived in equation (15) and (16).

$$E = E_c + E_f \quad (15)$$

$$E = E_c + \frac{1}{2} m^* (v_x^2 + v_y^2 + v_z^2) \quad (16)$$

Where;

m^* is electrons mass.

v_x, v_y, v_z is electrons velocity on xyz axes.

When consider the electrons and heat transport direction along x –axis, consequently E and T dependents on x –axis. Thus, gradient of Fermi–Dirac distribution along x –axis ($\nabla_r f_0$) are derived in equation (24).

$$\frac{\partial f_0}{\partial x} = \frac{\partial f_0}{\partial E} \frac{\partial E}{\partial x} + \frac{\partial f_0}{\partial E} \frac{\partial E}{\partial T} \frac{\partial T}{\partial x} \quad (17)$$

Defining;

$$y = \frac{1}{e^{\frac{E-E_f}{kT}} + 1} \quad (18)$$

$$\frac{\partial f_0}{\partial T} = \frac{\partial f_0}{\partial y} \left(-\frac{E - E_f}{kT^2} \right) \quad (19)$$

$$\frac{\partial f_0}{\partial E} = \frac{\partial f_0}{\partial y} \left(\frac{1}{kT} \right) \quad (20)$$

$$\frac{\partial f_0}{\partial E_f} = \frac{\partial f_0}{\partial y} \left(-\frac{1}{kT} \right) \quad (21)$$

$$\frac{\partial E}{\partial T} = \frac{E - E_f}{T} \quad (22)$$

$$\frac{\partial f_0}{\partial E} = -\frac{\partial f_0}{\partial E_f} \quad (23)$$

Thus;

$$\frac{\partial f_0}{\partial x} = -\frac{\partial f_0}{\partial E} \frac{\partial E_f}{\partial x} + \frac{E - E_f}{T} \frac{\partial f_0}{\partial E} \frac{\partial T}{\partial x} \quad (24)$$

The current density of the electron is calculated by summing all the charges, velocities and distribution of electron states as shown in equation (25)

$$J_e = \frac{1}{V} \sum_{k_x} \sum_{k_y} \sum_{k_z} (-e) v_x f \quad (25)$$

Where;

V is volume per all of state electrons $V = \frac{1}{L^3}$.

J_e is current density or current flux of electrons.

k is direction axes of electrons wave.

The summation equation is transformed into its integral form, following Fourier's law, using spherical coordinates, as shown in equation (27).

$$J_e = -\frac{1}{(L)^3} \int_{k_x=-\infty}^{\infty} \int_{k_y=-\infty}^{\infty} \int_{k_z=-\infty}^{\infty} e v_x f \frac{dk_x}{2\pi} \frac{dk_y}{2\pi} \frac{dk_z}{2\pi} \quad (26)$$

$$J_e = -\int_{k_x=-\infty}^{\infty} \int_{k_y=-\infty}^{\infty} \int_{k_z=-\infty}^{\infty} e v_x f \frac{1}{(2\pi)^3} dk_x dk_y dk_z \quad (27)$$

Defining;

$$dk_x dk_y dk_z = k^2 \sin \theta d\theta d\phi dk \quad (28)$$

$$V_1 = \left(\frac{2\pi}{L} \right)^3 \quad (29)$$

$$dN = \frac{4\pi k^2 dk}{V_1} = \frac{V k^2 dk}{2\pi} \quad (30)$$

$$dN = \frac{4\pi k^2 dk}{V_1} = \frac{V k^2 dk}{2\pi^2} \quad (31)$$

$$D(E) = \frac{dN}{V dE} = \frac{k^2 dk}{2\pi^2 dE} \quad (32)$$

Thus;

$$D(E)dE = \frac{k^2 dk}{2\pi^2} \quad (33)$$

$$\frac{D(E)}{4\pi} dE = \frac{k^2 dk}{(2\pi)^3} \quad (34)$$

Where;

θ, φ is spherical coordinate vertical and horizontal angles.

dN is different of number states (N) between spherical shield of k and $k + dk$ per unit volume of a state.

$D(E)$ is density state of electrons.

From equation (28) and (34), the equation (27) can be written as equation (35).

$$J_e = -\int_0^\infty \int_0^{2\pi} \int_0^\pi e(v \cos \theta) f \frac{D(E)}{4\pi} \sin \theta d\theta d\varphi dE \quad (35)$$

Then substituted equation (11) (f term) and (24) (F term) to equation (35).

$$J_e = -\int_0^\infty \int_0^{2\pi} \int_0^\pi e(v \cos \theta) \left(f_0 + \tau \left(v \cos \theta \frac{\partial f_0}{\partial x} + e\bar{E} \frac{dE}{dp} \frac{df_0}{dE} \right) \right) \frac{D(E)}{4\pi} \sin \theta d\theta d\varphi dE \quad (36)$$

From equation (15) and defining $dp = m dv$.

$$J_e = -\int_0^\infty \int_0^{2\pi} \int_0^\pi e(v \cos \theta) \left(f_0 + \tau v \cos \theta \left(\frac{\partial f_0}{\partial x} + e\bar{E} \frac{df_0}{dE} \right) \right) \frac{D(E)}{4\pi} \sin \theta d\theta d\varphi dE \quad (37)$$

$$J_e = -e \int_0^\infty \int_0^{2\pi} \int_0^\pi \left\{ v \cos \theta \sin \theta f_0 + \tau v^2 \cos^2 \theta \sin \theta \left(\frac{\partial f_0}{\partial x} + e\bar{E} \frac{df_0}{dE} \right) \right\} \frac{D(E)}{4\pi} d\theta d\varphi dE \quad (38)$$

Then, integrated θ term.

$$J_e = -e \int_0^\infty \int_0^{2\pi} \left\{ v f_0 \left(-\frac{\cos^2 \theta}{2} \right) \Big|_0^\pi + \tau v^2 \left(\frac{\partial f_0}{\partial x} + e\bar{E} \frac{df_0}{dE} \right) \left(-\frac{\cos^3 \theta}{3} \right) \Big|_0^\pi \right\} \frac{D(E)}{4\pi} d\varphi dE \quad (39)$$

$$J_e = -\frac{e}{6\pi} \int_0^\infty \int_0^{2\pi} \tau v^2 \left(\frac{\partial f_0}{\partial x} + e\bar{E} \frac{df_0}{dE} \right) D(E) d\varphi dE \quad (40)$$

Then, integrated φ term.

$$J_e = -\frac{e}{6\pi} \int_0^\infty \tau v^2 \left(\frac{\partial f_0}{\partial x} + e\bar{E} \frac{df_0}{dE} \right) D(E) (\varphi) \Big|_0^{2\pi} dE \quad (40)$$

$$J_e = -\frac{e}{3} \int_0^\infty \tau v^2 \left(\frac{\partial f_0}{\partial x} + e\bar{E} \frac{df_0}{dE} \right) D(E) dE \quad (41)$$

Then, substituted equation (24) in the equation (41).

$$J_e = -\frac{e}{3} \int_0^{\infty} \tau v^2 \left(-\frac{\partial f_0}{\partial E} \frac{\partial E_f}{\partial x} + \frac{E - E_f}{T} \frac{\partial f_0}{\partial E} \frac{\partial T}{\partial x} + e\bar{E} \frac{df_0}{dE} \right) D(E) dE \quad (42)$$

$$J_e = -\frac{e}{3} \int_0^{\infty} \tau v^2 \left(-\frac{\partial f_0}{\partial E} \frac{\partial E_f}{\partial x} + \frac{E - E_f}{T} \frac{\partial f_0}{\partial E} \frac{\partial T}{\partial x} + e\bar{E} \frac{df_0}{dE} \right) D(E) dE \quad (43)$$

Separated the equation (43) to couple term of temperature gradient and potential gradient as equation (44).

$$J_e = \frac{e}{3} \int_0^{\infty} \tau v^2 \frac{\partial f_0}{\partial E} D(E) dE \left(\frac{\partial E_f}{\partial x} - e\bar{E} \right) + \frac{e}{3T} \int_0^{\infty} \tau v^2 (E - E_f) \frac{\partial f_0}{\partial E} D(E) dE \left(-\frac{\partial T}{\partial x} \right) \quad (44)$$

Due to electrochemical potential is defined as equation (45).

$$\Phi = \frac{E_f}{q} - V_{external} = -\left(\frac{E_f}{e} - V_{external} \right) \quad (45)$$

The current density of the electron can rewrite as equation (47).

$$J_e = \frac{e^2}{3} \int_0^{\infty} \tau v^2 \frac{\partial f_0}{\partial E} D(E) dE \left(-\frac{\partial \Phi}{\partial x} \right) + \frac{e}{3T} \int_0^{\infty} \tau v^2 (E - E_f) \frac{\partial f_0}{\partial E} D(E) dE \frac{\partial T}{\partial x} \quad (46)$$

$$J_e = L_{11} \left(-\frac{\partial \Phi}{\partial x} \right) + L_{12} \left(-\frac{\partial T}{\partial x} \right) \quad (47)$$

Defining;

$$L_{11} = \frac{e^2}{3} \int_0^{\infty} \tau v^2 \frac{\partial f_0}{\partial E} D(E) dE \quad (48)$$

$$L_{12} = \frac{e}{3T} \int_0^{\infty} \tau v^2 (E - E_f) \frac{\partial f_0}{\partial E} D(E) dE \quad (49)$$

Defining;

$$\sigma = L_{11} = \frac{e^2}{3} \int_0^{\infty} \tau v^2 \frac{\partial f_0}{\partial E} D(E) dE \quad (50)$$

Where;

σ is electrical conductivity.

The Seebeck coefficient is evaluated using equation (47) when the system is in a steady state as $J_e = 0$ (open circuit condition).

$$0 = L_{11} \left(-\frac{\partial \Phi}{\partial x} \right) + L_{12} \left(-\frac{\partial T}{\partial x} \right) \quad (51)$$

$$\alpha = -\frac{\partial \Phi / \partial x}{\partial T / \partial x} = \frac{L_{12}}{L_{11}} \quad (52)$$

The electron current transport equation can be rewritten to incorporate electrical conductivity and Seebeck coefficient along equation (47), (50) and (52) as equation (53).

$$J_e = \sigma \left(-\frac{\partial \Phi}{\partial x} \right) - \alpha \sigma \frac{\partial T}{\partial x} \quad (53)$$

For r space;
$$J_e = \sigma(-\Delta\Phi) - \alpha\sigma\Delta T \quad (54)$$

Based on equations (50) and (52), the equation can be used to predict electrical conductivity and Seebeck coefficient of thermoelectric materials.

The equation described electron flow along Boltzmann transport equation and the Fermi-Dirac distribution. Similarly, heat flow is derived using the same process as for the electron current density. The heat flow is derived from the first law of thermodynamic, as shown in equation (55).

$$dU = dQ + E_f dn \quad (55)$$

$$dQ = dU - E_f dn \quad (56)$$

$$dJ_Q = dJ_U - dJ_n \quad (57)$$

Where;

U is energy of system

Q is heat of system

n is number of particles

J_Q is heat flux

J_U is energy flux

J_n is particles flux

The energy density can be calculated by integrating of all energy E along x-axis direction, as shown in equation (58).

$$J_U = \int_{-\infty}^{\infty} \int_{-\infty}^{\infty} \int_{-\infty}^{\infty} E v_x f dv_x dv_y dv_z \quad (58)$$

The particle density can be calculated by integrating of all energy E_f along x-axis direction, as shown in equation equation (59).

$$J_n = \int_{-\infty}^{\infty} \int_{-\infty}^{\infty} \int_{-\infty}^{\infty} E_f v_x f dv_x dv_y dv_z \quad (59)$$

Thus, the heat density consists of energy and particle density integration is shown in equation (60).

$$J_Q = \int_{-\infty}^{\infty} \int_{-\infty}^{\infty} \int_{-\infty}^{\infty} (E - E_f) v_x f dv_x dv_y dv_z \quad (60)$$

The heat density for thermoelectric system is determined by the electron carrier, the distribution function J and Fermi–Dirac distribution. Consequently, equation (60) is derived using equation (11) to (46). The heat density J_Q is expressed in equation (61).

$$J_Q = L_{21} \left(-\frac{\partial \Phi}{\partial x} \right) + L_{22} \left(-\frac{\partial T}{\partial x} \right) \quad (61)$$

Defining;

$$L_{21} = \frac{e}{3} \int_0^\infty v^2 (E - E_f) \frac{\partial f_0}{\partial E} D(E) dE \quad (62)$$

$$L_{22} = -\frac{e}{3T} \int_0^\infty v^2 (E - E_f)^2 \frac{\partial f_0}{\partial E} D(E) dE \quad (63)$$

The relation between L_{12} and L_{22} connection originally described by Lars Onsager, known as the “Onsager relations”.

$$L_{21} = TL_{12} \quad (64)$$

When the chemical potential term is eliminated, the current density and heat density equation reveal the correlation of heat flow, as shown in equation (65).

$$J_Q = \frac{L_{21}}{L_{12}} J_e + (L_{22} - \frac{L_{12}L_{21}}{L_{11}}) \left(-\frac{\partial T}{\partial x} \right) \quad (65)$$

Defining;

$$\Pi = \frac{L_{21}}{L_{11}} \quad (66)$$

$$k = (L_{22} - \frac{L_{12}L_{21}}{L_{11}}) \quad (67)$$

Where;

κ is thermal conductivity.

The heat transport equation due to electron carrier can be rewritten to include thermal conductivity and the Peltier coefficient, as show in equation (65), (66) and (67), and is expressed in equation (68).

$$J_Q = \Pi J_e - \kappa \left(\frac{\partial T}{\partial x} \right) \quad (68)$$

For r space;

$$J_e = \Pi J_e - \kappa \Delta T \quad (69)$$

Based on equation (66) and (67), the Peltier coefficient and thermal conductivity of thermoelectric materials can be calculated. The coupled transport processes of the thermoelectric effect and the associated coefficient parameters have been derived and defined. The efficiency of thermoelectric materials and devices was then

calculated to optimize the maximal performance of electrical generators and cooling systems. Thomson effect (4) was considered in determining the maximal performance of thermoelectric materials, using the Domenicali equation (Thomson relations $\dot{Q} = -\kappa\Delta^2T$) (Rowe, 2018; Zlatic and Monnier, 2014).

$$\dot{Q} = -\kappa\Delta^2T = \frac{J^2}{\sigma} - J\left(\frac{T\partial\alpha}{\partial T}\right)\Delta T \quad (70)$$

It is assumed that heat transfer occurs along the x-axis, with the cold side of the materials at $x_0 = 0$, T_0 and the hot side end at $x_1 = l$, T_1 . As a result, the term of $J\left(\frac{T\partial\alpha}{\partial T}\right)\Delta T$ is eliminated because α don't change within a material. The equation (70) can be rewrite as equation (71).

$$-\kappa \frac{\partial^2 T}{\partial^2 x} = \frac{J^2}{\sigma} \quad (71)$$

$$-\int \kappa \frac{\partial^2 T}{\partial^2 x} \partial x = \int \frac{J^2}{\sigma} \partial x \quad (72)$$

$$-\kappa \frac{\partial T}{\partial x} = \frac{J^2}{\sigma} x + F \quad (73)$$

$$-\int \kappa \frac{\partial T}{\partial x} \partial x = \int \left(\frac{J^2}{\sigma} x + F \right) \partial x \quad (74)$$

$$-\kappa T(x) = \frac{J^2 x^2}{2\sigma} + Fx + G \quad (75)$$

At condition $x_0 = 0$, T_0 , the parameter G is shown in equation (76).

$$G = -\kappa T_0 \quad (76)$$

Thus;

$$-\kappa T(x) = \frac{J^2 x^2}{2\sigma} + Fx - \kappa T_0 \quad (77)$$

At condition $x_1 = l$, T_1 .the parameter F is shown in equation (78).

$$F = -\frac{J^2 l}{2\sigma} - \frac{\kappa}{l}(T_1 - T_0) \quad (78)$$

Thus;

$$-\kappa T(x) = \frac{J^2 x^2}{2\sigma} - \frac{J^2 lx}{2\sigma} - \frac{\kappa}{l}(T_1 - T_0)x - \kappa T_0 \quad (79)$$

Defining;

$$K = \frac{\kappa A}{l} \quad (80)$$

$$R = \frac{l}{\sigma A} \quad (81)$$

$$J = \frac{I}{A} \quad (82)$$

Where;

- F is thermal conductance
- G is electrical resistance
- K is thermos conductance
- R is electrical resistance
- A is surface area of the materials
- l is length of the materials

Substituted equation (80), (81) and (82) in equation (79);

$$T(x) = -\frac{I^2 R x^2}{2Kl^2} + \frac{I^2 R x}{2Kl} + \left(\frac{T_1 - T_0}{l}\right)x + T_0 \quad (83)$$

Then;

$$\frac{\partial T(x)}{\partial x} = \frac{RI^2}{2Kl} \left(1 - \frac{2x}{l}\right) + \frac{T_1 - T_0}{l} \quad (84)$$

Substituted equation (83) in equation (68) to get heat transport.

$$J = \Pi J - \kappa \Delta T \quad (85)$$

$$J_Q = T \alpha J_e - \kappa \Delta T \quad (86)$$

At condition heat transfer along in x-axis, $x_0 = 0$, T_0 , the equation (86) is changed.

$$Q_0 = \alpha I T_0 - K(T_1 - T_0) - \frac{RI^2}{2} \quad (87)$$

Defining;

$$J_Q = \frac{Q}{A} \quad (88)$$

The maximal heat transfer depended on current I , Then optimal current that yields maximal heat transfer is determined by taking the derivative of equation (87) with dI

$$\frac{\partial Q_0}{\partial I} = \frac{\partial \left(\alpha I T_0 - K(T_1 - T_0) - \frac{RI^2}{2} \right)}{\partial I} \quad (89)$$

$$0 = \alpha T_0 - RI \quad (90)$$

$$I_{op} = \frac{\alpha T_0}{R} \quad (91)$$

Substituted I_{op} in equation (87).

$$Q_0 = \frac{\alpha^2 T_0^2}{2R} - K(T_1 - T_0) \quad (92)$$

Under this condition, the heat source will transfer until reach $Q_0 = 0$. The maximum possible different temperature $(T_1 - T_0)$ at the other end of a materials is shown in equation (95).

$$(T_1 - T_0)_{\max} = \frac{\alpha^2}{2RK} T_0^2 \quad (93)$$

$$(T_1 - T_0)_{\max} = \frac{\alpha^2 \sigma}{2\kappa} T_0^2 \quad (94)$$

$$(T_1 - T_0)_{\max} = Z T_0^2 \quad (95)$$

Defining;

$$Z = \frac{\sigma \alpha^2}{\kappa} \quad (96)$$

Where;

Z is the figure of merit.

The figure of merit is a widely used parameter to indicate the performance of thermoelectric materials.

2.1.3 Effects in a magnetic field

Normally, electrical charges are horizontal forced as move through in magnetic field. As a result, the properties of thermoelectric effects can change when a magnetic field is applied. The influence of magnetic field on thermoelectric effects is known as “Thermogalvanomagnetic effects”, which impact the performance of thermoelectric module. The thermogalvanomagnetic effects is illustrated in Figure 4. The variation in Seebeck coefficient when the magnetic field is reversed is referred to as the “Umkehr effect”. The Umkehr effect is deployed by equation (97).

$$\Pi(\mathbf{B}) = \mathbf{T} \alpha(-\mathbf{B}) \quad (97)$$

Where;

\mathbf{B} is a magnetic field

When a magnetic field is applied to a system, an electric field will appear perpendicular to both electrical current and magnetic field. This phenomenon is known as “Hall effect”. However, the transverse voltage that arises in a magnetic field due to a longitudinal temperature gradient or heat flow is called “Nernst effect”. Unlike the Hall effect, the Nernst effect is independent of whether the charge carriers are positive or negative. The Nernst coefficient (N) is defined by equation (98).

$$|N| = \frac{dV/dy}{B_z dT/dx} \quad (98)$$

Where;

N is Nernst coefficient.

dV/dy is a derivative of transverse electric field.

x, y and z are Cartesian coordinate system.

Moreover, Ettingshausen refers to the generation of a transverse temperature gradient in the presence of a transverse magnetic field and a longitudinal electric current. The Ettingshausen coefficient (E_p) is defined by equation (99).

$$E_p = \frac{dT/dy}{i_x B_z} \tag{99}$$

Where;

E_p is Ettingshausen coefficient.

dT/dy is a derivative of temperature.

The correlation between Ettingshausen effect and Nernst effect is represented in equation (100).

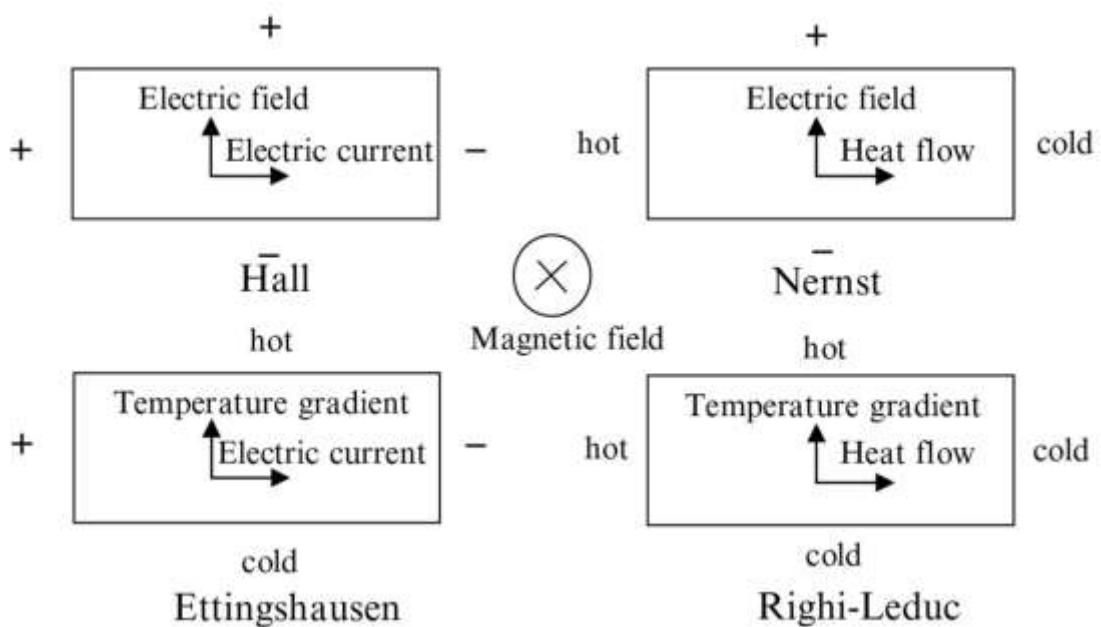


Figure 4 The thermogalvanomagnetic effects with different directions of involved parameters (Goldsmid, 2010).

$$E_p \kappa = NT \tag{100}$$

The final thermogalvanomagnetic effects is “Righi-Leduc effect” which refers to transverse temperature gradient generated by perpendicular heat flow. The Righi-Leduc coefficient (R_s) is defined by equation (101).

$$R_s = \frac{dT/dy}{B_z dT/dx} \quad (101)$$

Where;

R_s is Righi–Leduc coefficient.

2.1.4 Transport effects

The thermoelectric phenomena are reversible process according to thermodynamics principles, but thermoelectric parameters, such as electrical resistance and thermal conduction, are irreversible. However, reversibility can be expressed in terms of the derivatives of Seebeck coefficient, thermal conduction, and electrical resistances. The electrical current depend on electrical conductivity, electrical voltage and the ratios of length to cross-sectional area, as shown in equation (102).

$$I = \frac{\sigma VA}{L} \quad (102)$$

Where;

A is cross-sectional area.

L is length

V is applied voltage

Moreover, the thermal conductivity is defined by the equation (103).

$$q = -\frac{\kappa A \Delta T}{L} \quad (103)$$

Where;

q is rate of heat flow.

The thermoelectric coefficients, along with electrical and thermal conductivities, are considered key transport properties of a materials. These properties are typically temperature-dependent, and the variation temperature has a significant impact on thermoelectric generation.

2.1.5 Thermoelectric refrigerators

The performance of a refrigerators involves applying an external electrical voltage to the end of a thermoelectric couple subsequent occur heat source (T_h) and cold source or heat pump (T_c). A thermoelectric refrigerator consisting of p-n couple is demonstrated in Figure 5.

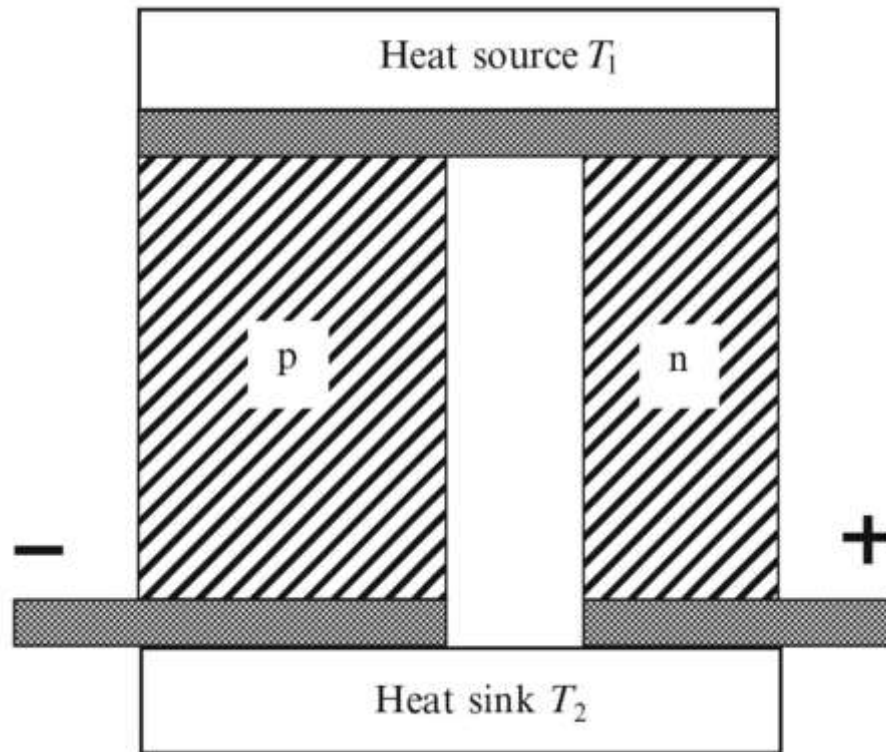


Figure 5 Illustration of model a couple p-n pair refrigerator (Goldsmid, 2010).

When an electrical current is applied to thermoelectric refrigerator, or in the case of Peltier cooling, subsequent heat flow through the p-n couple $(\alpha_p - \alpha_n)IT_h$, which using Kelvin relation in equation (3) eliminate Peltier coefficient in equation (2). Heat conduction creates resistance to the heat pump as $(T_h - T_c)(\kappa_p + \kappa_n)$. The heat pump is also opposed by half of Joule heating, similar to a Carnot cycle as $I^2(R_p + R_n)/2$. The rate of the heat pump can be express in equation (104).

$$q = (\alpha_p - \alpha_n)IT_h - (T_h - T_c)(\kappa_p + \kappa_n) - \frac{I^2(R_p + R_n)}{2} \quad (104)$$

The rate of electrical power usage also expresses in equation (105).

$$P_{out} = (\alpha_p - \alpha_n)I(T_h - T_c) - I^2(R_p + R_n) \quad (105)$$

Where;

P_{out} is electrical power.

Therefore, the performance of a refrigerator, measured as the coefficient of performance (COP), can be determined by dividing the heat flow described in equation (104) by electrical power usage give in equation (105). The COP is represented in equation (106).

$$\phi = \frac{(\alpha_p - \alpha_n)IT_h - (T_h - T_c)(\kappa_p + \kappa_n) - \frac{I^2(R_p + R_n)}{2}}{(\alpha_p - \alpha_n)I(T_h - T_c) - I^2(R_p + R_n)} \quad (106)$$

Where;

ϕ is coefficient of performance (COP).

2.1.6 Thermoelectric generators

Thermoelectric generators, based on Seebeck effect, are used to directly convert heat into electrical current. These thermoelectric generators operate using a model of a p-n couple generator, as shown in Figure 6. The couple p-n generator is connected to a load resistance R_L , generating electricity through the temperature difference between the two end of the generator. The generated electrical power is delivered to the load resistance, and the efficiency η is calculated as the ratio of the electrical output power to the rate of heat drawn. The heat drawn is flowing of heat due to thermal conduction along the p-n couple generator. Total rate of heat flow is expressed in equation (107).

$$q = (\alpha_p - \alpha_n)IT_h + (T_h - T_c)(\kappa_p + \kappa_n) \quad (107)$$

While the electromotive force (EMF) give electrical current following equation (108).

$$I = \frac{(\alpha_p - \alpha_n)(T_h - T_c)}{R_p + R_n + R_L} \quad (108)$$

Then, the electrical output power is;

$$P_{out} = I^2 R_L = \left[\frac{(\alpha_p - \alpha_n)(T_h - T_c)}{R_p + R_n + R_L} \right]^2 R_L \quad (109)$$

The efficiency η is the ratio of electrical output power to the rate of heat drawn, equation (109) divide by equation (107).

$$\eta = \frac{\left[\frac{(\alpha_p - \alpha_n)(T_h - T_c)}{R_p + R_n + R_L} \right]^2 R_L}{(\alpha_p - \alpha_n)IT_h + (T_h - T_c)(\kappa_p + \kappa_n)} \quad (110)$$

When;

$$M = \frac{R_L}{R_p + R_n} \quad (111)$$

Finally, the efficiency η can be deploy by equation (112).

$$\eta = \frac{(T_h - T_c)(M - 1)}{T_h \left(M + \frac{T_c}{T_h} \right)} \quad (112)$$

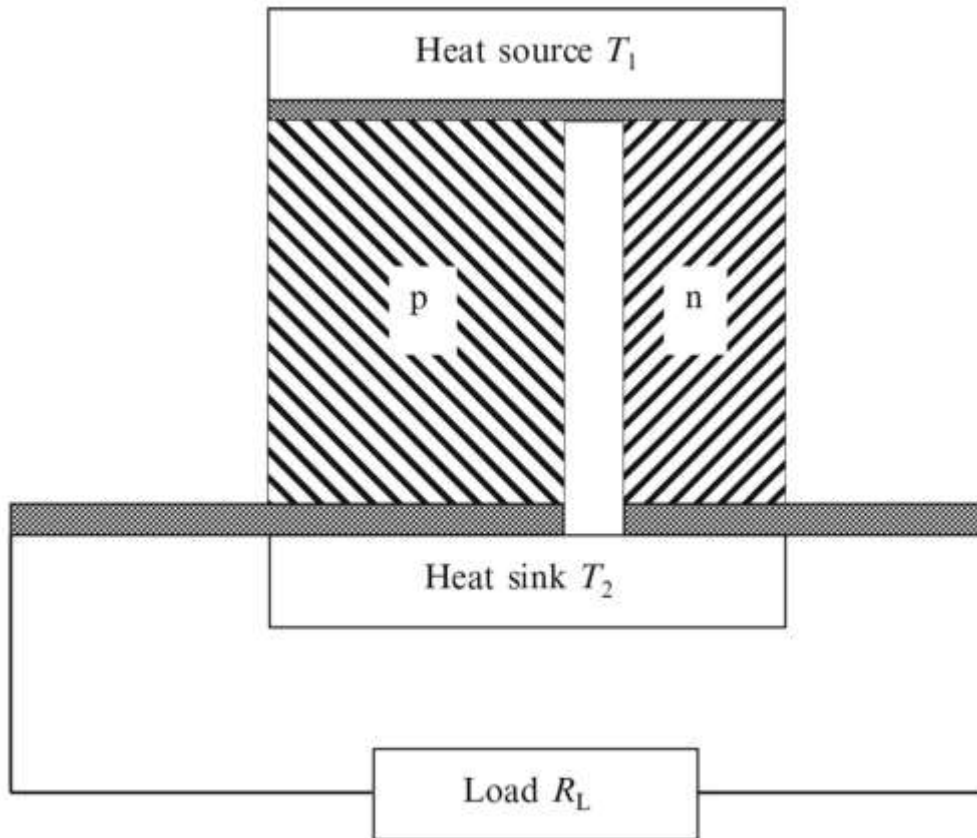


Figure 6 Illustration of model a couple p-n generator (Goldsmid, 2010).

2.2 Thermoelectric materials

2.2.1 Thermoelectric materials

Normally, thermoelectric materials are typically classified into n-type and p-type materials, based on its charge carrier and ability to generate heat and cold at

the couple end of the materials. For n-type thermoelectric materials, there is a temperature difference between the two ends, an electric field is induced, with the direction from the hot side (+) to the cold side (-) and subsequent in a high density of electron at cold side and a low density of electrons at hot side. Conversely, in p-type thermoelectric materials, the electric field is induced in the opposite direction, from the cold side (+) to the hot side (-) and subsequent in a high density of holes (low density of electron) at cold side and a low density of hole at hot side (high density of electrons). The behaviour of n-type and p-type of thermoelectric materials is shown in Figure 7.

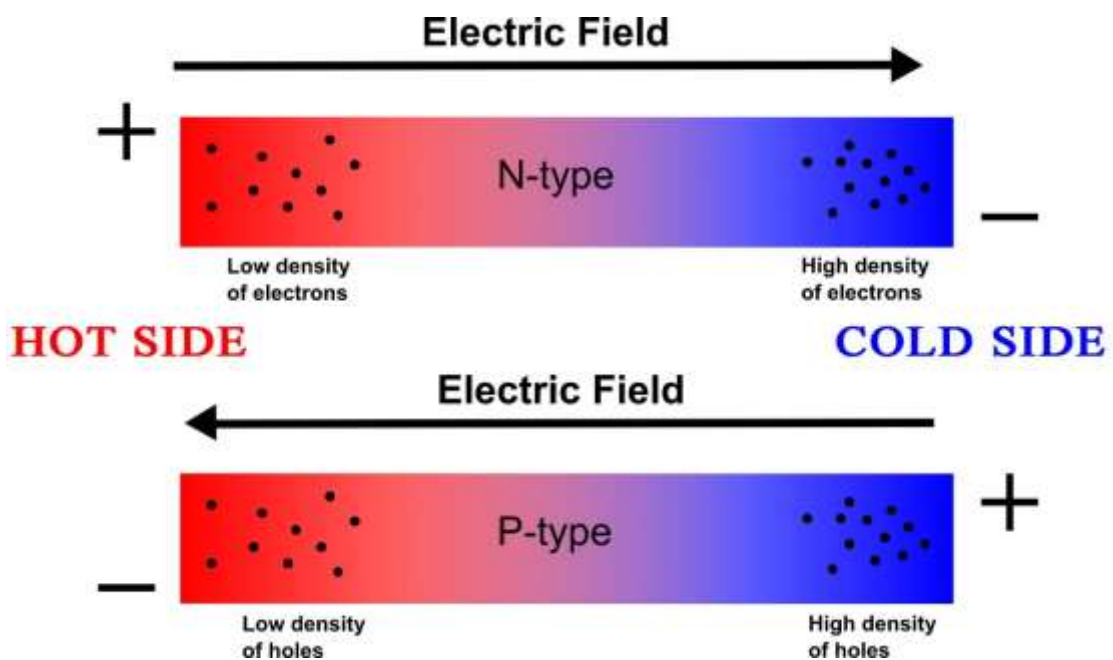


Figure 7 Illumination of n-type and p-type of thermoelectric materials behaviour (Nabilasamiron, 2012).

The optimal thermoelectric materials for converting heat into electrical current at various operating temperature are evaluated based on thermoelectric properties, such as Seebeck coefficient, thermal conductivity, electrical conductivity, as well as the dimensionless figure of merit (ZT) described in equation (96). According to Marta Rull's report, a summary of the performance of p-type and n-type of thermoelectric materials across different operating temperatures is shown in Figure 8 (Rull-Bravo *et al.*, 2015). Moreover, Table 1 lists various thermoelectric materials, operating temperatures, power factor, synthesis method and ZT . The excellent thermoelectric materials, characterized by a high ZT (>1) and great power factor, i. e., $\text{Bi}_x\text{Sb}_{2-x}\text{Te}_3$, $\beta\text{-Zn}_4\text{Sb}_3$, $\beta\text{-Cu}_4\text{Se}$, $(\text{GeTe})_{0.85}(\text{ASbTe}_2)_{0.15}$, Na-Pb-Sb-Te , PbTe-rTe-Na , $\text{Yb}_{14}\text{Mn}_{1-x}\text{Al}_x\text{Sb}_{11}$,

$\text{Bi}_2\text{Te}_{3-x}\text{Se}_x$, $\text{Mg}_2\text{Si-Mg}_2\text{Sn}$, $\text{AgPb}_m\text{SbTe}_{2+m}$, $\text{PbTe-Ag}_2\text{Te-La}_{0.08}\text{La}_{0.05}\text{Yb}$, P-doped SiGe , $\text{Bi}_{0.92}\text{Pb}_{0.08}\text{CuSeO}$, $\text{Bi}_{0.875}\text{Ba}_{0.125}\text{CuSeO}$, SnS , SnSe and Ag_2Se . However, in light of the global energy crisis and the motivation discussed in the chapter I to recycle industrials waste heat, the most suitable thermoelectric materials for temperatures corresponding to waste heat about 200–400 °C (Minea, 2007) include $\beta\text{-Zn}_4\text{Sb}_3$ (Caillat *et al.*, 1997), SnSe (Gainza *et al.*, 2020), Na-Pb-Sb-Te (salt) (Poudeu *et al.*, 2006), SnS (Asfandiyar *et al.*, 2017), PbTe-SrTe-Na (Biswas *et al.*, 2012), $(\text{GeTe})_{0.85}(\text{AgSbTe}_2)_{0.15} + 2\%\text{Dy}$ (Levin *et al.*, 2012) in p-type thermoelectric materials, and $\text{Ba}_{0.08}\text{La}_{0.05}\text{Yb}_{0.04}\text{Co}_4\text{Sb}_{12}$ (skutterudite) (Shi *et al.*, 2011), $\text{Mg}_2\text{Si}_{1-x}\text{Sn}_x$ (Liu *et al.*, 2012), $\text{AgPb}_{18}\text{SbTe}_{20}$ (LAST) (Hsu *et al.*, 2004), ZnAl_2O_4 (Jood *et al.*, 2011), $\text{In}_{2-x}\text{Ce}_x\text{O}_3$ (Lan *et al.*, 2015), $\text{Ca}_3\text{Co}_4\text{O}_9$ (Zhang *et al.*, 2020), $\text{Bi}_{0.875}\text{Ba}_{0.125}\text{CuSeO}$ (Sui *et al.*, 2013), $\text{Bi}_{0.92}\text{Pb}_{0.08}\text{CuSeO}$ (Wang *et al.*, 2016) in n-type thermoelectric materials.

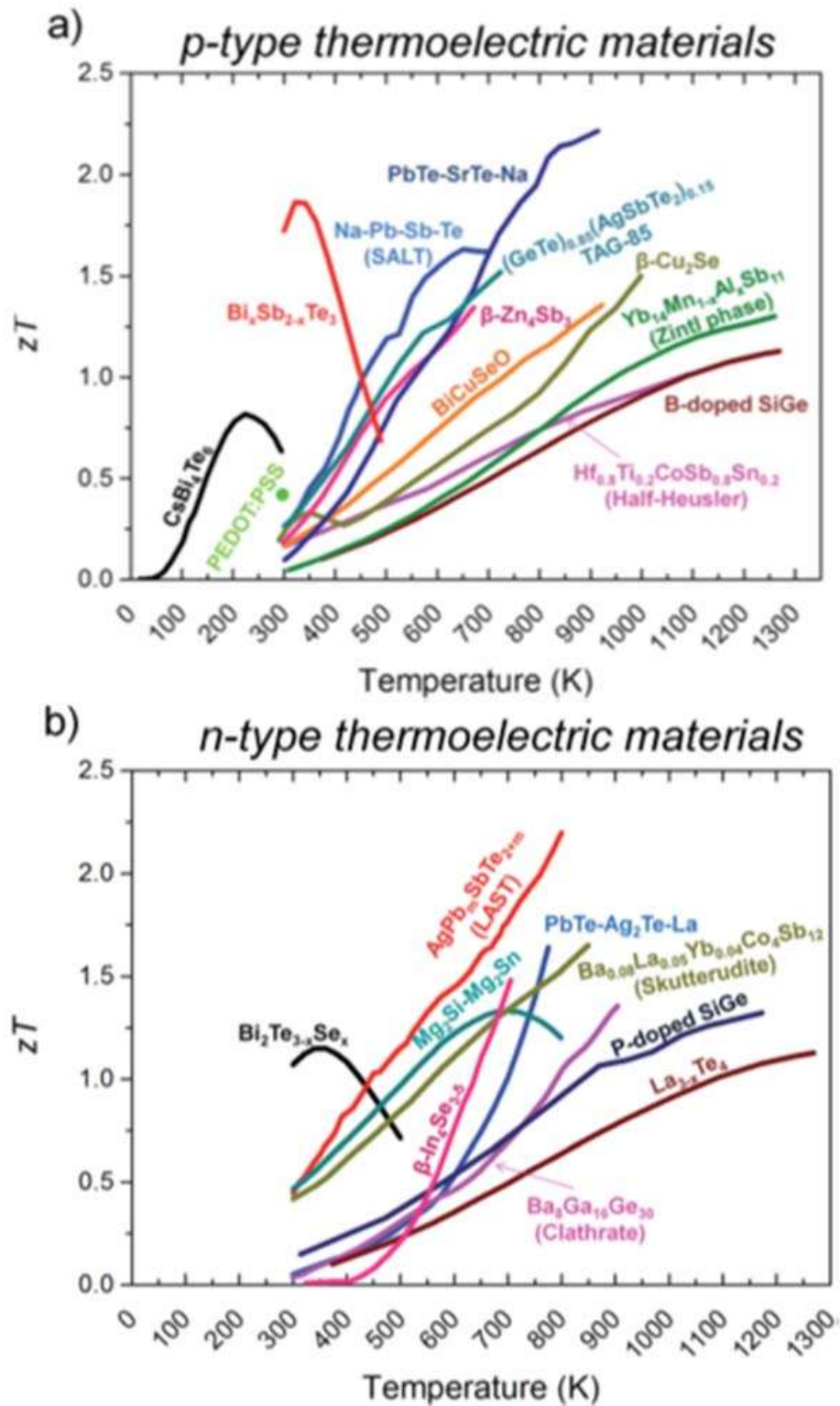


Figure 8 Summary of ZT as a functional temperature of p-type and n-type of thermoelectric materials, a) p-type thermoelectric materials and b) n-type thermoelectric materials (Rull-Bravo *et al.*, 2015).

Table 1 List of thermoelectric materials versus operating temperatures, power factor, synthesis method and ZT.

Materials	ZT	Type	Temp.(K)	Power Factor ($\mu\text{Wcm}^{-1}\text{K}^{-2}$)	Synthesis Method	Reference
Ag_2Se	1.2	N	273	24.4	Magnetron sputtering	(Perez-Taborda <i>et al.</i> , 2018)
$\text{Ag}_2\text{Se}_{1.06}$	0.84	N	300	30.1	Spark plasma sintering	(Mi <i>et al.</i> , 2014)
$\text{Ag}_2\text{S}_{0.5}\text{Se}_{0.5}$	0.44	N	300	–	Spark plasma sintering	(Liang <i>et al.</i> , 2019)
$\text{Ag}_{1.9}\text{Sn}_{0.1}\text{Se}$	0.9	N	300	4.5	Wet chemical process	(Tee <i>et al.</i> , 2022)
Bi_2Te_3	0.4	P	300	–	–	(Zhang <i>et al.</i> , 2013)
Bi_2Te_3	0.7	P	400	–	Arc melting method	(Gharsallah <i>et al.</i> , 2016)
Zn_4Sb_3	0.81	P	600	–	Mechanical Alloying	(Lee and Lin, 2018)
Zn_4Sb_3	1.36	P	600	–	Hot pressing	(Kunioka <i>et al.</i> , 2018)
SnSe	1.57	P	300–700	–	Arc melting method	(Gainza <i>et al.</i> , 2020)
SnS	2.6	P	900	0.75	Mechanical Alloying	(Asfandiyar <i>et al.</i> , 2017)
ZnAl_2O_4	0.44	N	1000	0.18	Microwave-stimulated	(Jood <i>et al.</i> , 2011)
$\text{In}_{2-x}\text{Ce}_x\text{O}_3$	0.47	N	1200	2.5	Spark plasma sintering	(Lan <i>et al.</i> , 2015)

Table 2 list of thermoelectric materials versus operating temperatures, power factor, synthesis method and ZT. (Continued)

Materials	ZT	Type	Temp.(K)	Power Factor ($\mu\text{Wcm}^{-1}\text{K}^{-2}$)	Synthesis Method	Reference
$\text{Ca}_3\text{Co}_4\text{O}_9$	0.40	P	900	–	Spark plasma sintering	(Zhang <i>et al.</i> , 2020)
$\text{Bi}_{0.875}\text{Ba}_{0.125}$ CuSeO	1.4	P	900	6.3	Solid state reaction route	(Sui <i>et al.</i> , 2013)
$\text{Bi}_{0.92}\text{Pb}_{0.08}\text{Cu}$ uSeO	1.1	P	800	7.3	Solid state reaction route	(Wang <i>et al.</i> , 2016)

Among the materials mentioned, β -Zn₄Sb₃ stands out as an excellent thermoelectric material in the temperature range of 200 – 400 °C (473.15 – 673.15 K) due to its high ZT value, availability of inexpensive elemental sources, low toxicity, and simple crystalline structure. The thermoelectric materials of Zn–Sb system include ZnSb, Zn₃Sb₂ and Zn₄Sb₃, each exhibiting unique thermoelectric properties. The study of the Zn-Sb system in thermoelectric itinerary began when T. J. Seebeck surveyed elements and alloy materials, include correlation of electrical production (potential voltage) and temperatures differences in various materials, including ZnSb alloy (Seebeck, 1895). Later, Zn₃Sb₂ were reported an optimal ratio of Zn:Sb for maximizing Zn₃Sb₂ crystalline (Mönkemeyer, 1905), and its thermoelectric properties were further explored (Beer and Cochran, 1952). The phase diagram and structural polymorphs of Zn₄Sb₃ namely α -Zn₄Sb₃, β -Zn₄Sb₃ and γ -Zn₄Sb₃, were studied by Mayer K. W. in 1978 (Mayer *et al.*, 1978). The thermoelectric properties of β -Zn₄Sb₃ have been investigated since the 19th century, as report by Tapiero M., Spitzer D., and Ugai Ya. (Tapiero *et al.*, 1985; Spitzer, 1970; Ugai *et al.*, 1963). Among the Zn–Sb system materials, the β -Zn₄Sb₃ is particularly noteworthy for its excellent thermoelectric performance in the intermediate temperature range about 200–400 °C (473.15–673.15 K), achieving a maximum figure of merit (ZT) approximately 1.3 (Caillat *et al.*, 1997).

2.2.2 Process synthesis

The thermoelectric materials were synthesized using various process depending on the structural materials involved. For example, oxide materials were prepared using the sol–gel method (a wet chemical process) (Tee *et al.*, 2022), alloy materials were synthesized via solid–state reaction, mechanical alloying, and quenching methods (Lee and Lin, 2018; Mirela *et al.*, 2015), thin films were created using magnetron sputtering (Perez-Taborda *et al.*, 2018), ceramic bulk materials were produced through hot pressing (Kunioka *et al.*, 2018).

Sol–gel method

Sol–gel method is a chemical process used to synthesis a wide range of oxide materials, including thermoelectric materials with oxide structure like $\text{Ca}_3\text{Co}_4\text{O}_9$, $\text{In}_{2-x}\text{Ce}_x\text{O}_3$ and ZnAl_2O_4 . In this method, the initial materials are dissolved in a liquid solvent, and the solution is then heated and stirred to form a gel. Once the gel has dried, the resulting powders is calcined under optimal conditions specific to each material. This process successfully produces the desired materials. Figure 9 illustrates a schematic of sol–gel method.

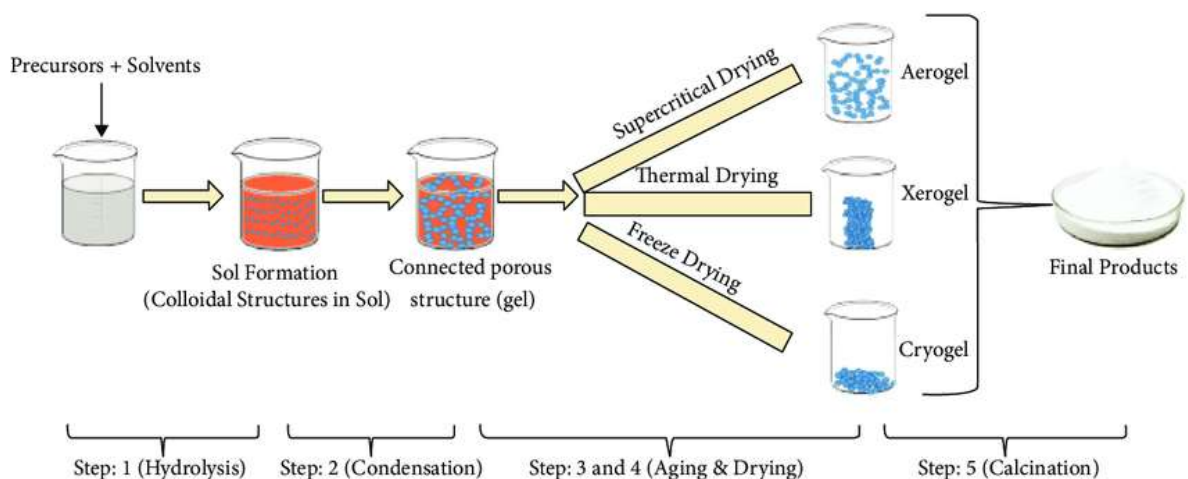


Figure 9 Schematic of sol–gel method step by step (Bokov *et al.*, 2021).

Hot pressing technique

Hot pressing technique combines synthesis and sintering into a single process. In this method, the starting materials are prepared in the optimal stoichiometric ratio before being placed into a graphite mold. The mold is then subjected to suitable pressure using a hydraulic system and heated to an optimal temperature, allowing

crystallites to form and the material to be sintered into a bulk pellet. Lately, the sintered ceramic pellet of the desired materials is done. A Schematic diagram illustrating of the hot pressing technique is shown in Figure 10.

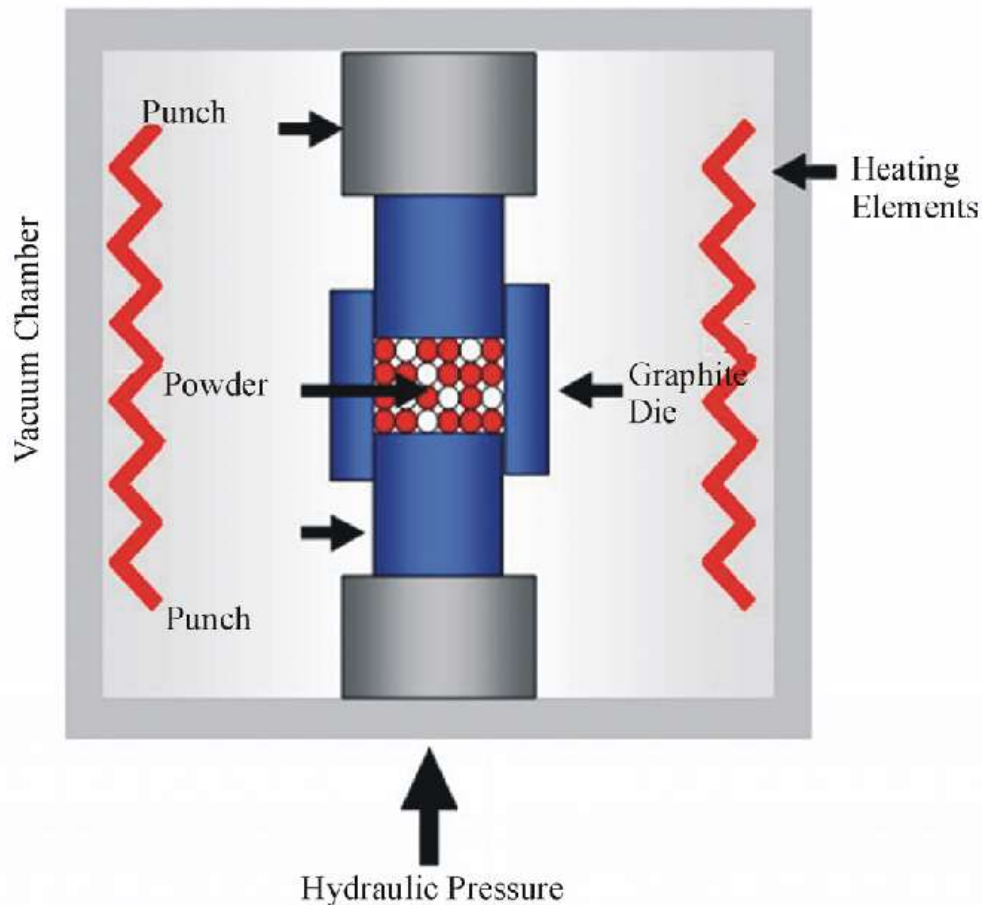


Figure 10 Schematic diagram illustrating the hot pressing technique (Moustafa *et al.*, 2011).

Magnetron sputtering

Magnetron sputtering is widely used to fabricate film for coating substrate. This technique operates in a vacuum environment to facilitate plasma formation, utilizing gas ions such as Ar, N₂, O₂, He, or H₂. In this process, a bulk materials (target) is subjected to high-energy ionized gas, which bombards the target materials, causing its atoms to be ejected. These ejected ions are then deposited onto the substrate, forming a thin film, guided by the electric field between the anode and cathode. Magnetron sputtering is typically categorized into DC magnetron sputtering and Pulse-DC magnetron sputtering, as illustrated in Figure 11.



Figure 11 DC magnetron sputtering and. Pulsed DC magnetron sputtering (Vaccoat, 2024).

Spark plasma sintering

Spark plasma sintering (SPS) is similar to the hot pressing technique. However, instead of conventional heating, SPS directly heats the material powders using a pulsed direct electrical current at low voltage. An illustration of SPS technique is shown in Figure 12.

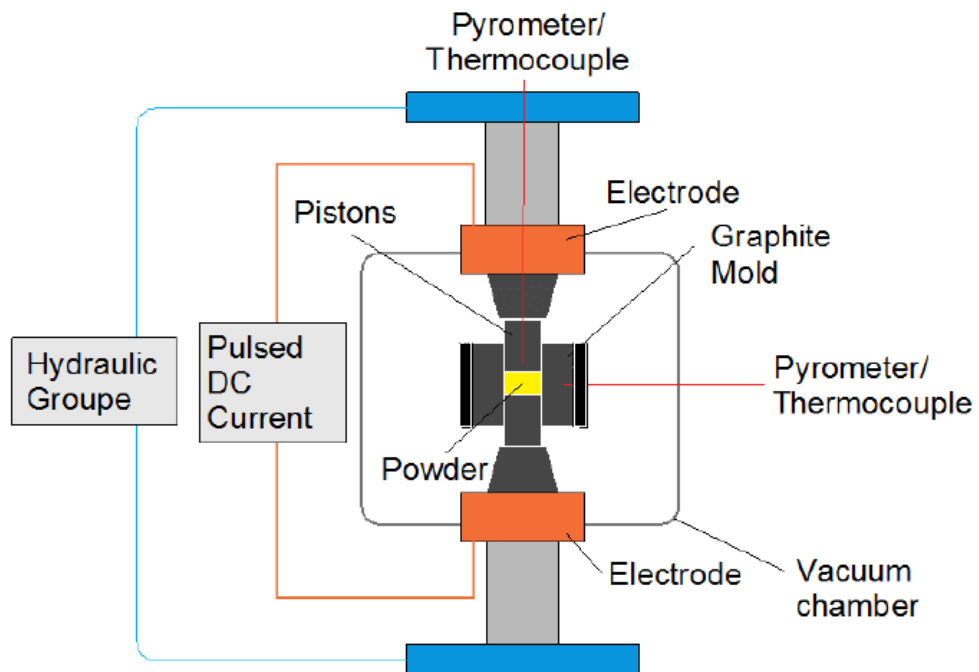


Figure 12 Illustration of Spark plasma sintering technique (Max Planck Institutes).

Quenching process

The Quenching process involves rapidly cooling a material after melting or calcination. First, the precursor is sealed in a quartz tube and then subjected to melting or calcined at an optimal temperature. Afterward, the quartz tube is quickly submerged in water to cool the sample rapidly. This process prevents the recrystallization of polymorph phases during the cooling phase of calcination process. The general overview of the quenching process is illustrated in Figure 13.

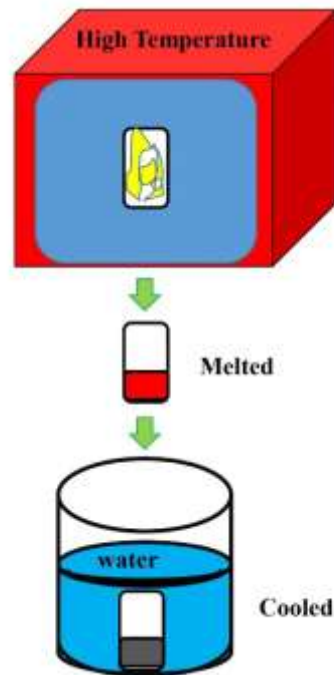


Figure 13 Illustration of quenching process after melting process.

Mechanical alloying

Mechanical alloying (MA) is a key step in solid state reaction process, involving the cyclical welding, fracturing, and re-welding of powders particles in a ball mill or a high-energy ball mill chamber. Typically, the MA process is used to mix initial sample powders, flatten and crack bulk sample, and weld powders particles together. This technique is widely used in the preparation of alloy materials. An illustration of the mechanical alloying (MA) is shown in Figure 14.

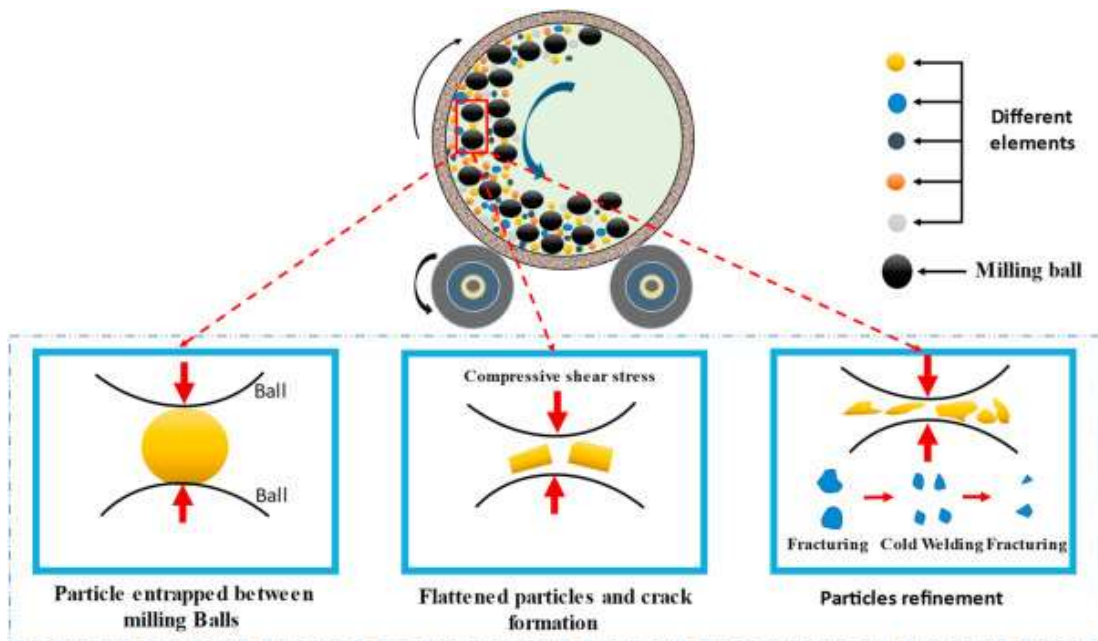


Figure 14 Mechanical alloying with flat and crack bulk sample (Kumar *et al.*, 2022).

Solid-state reaction

Solid-state reaction is a synthesis method used to produce polycrystalline materials. The reaction typically occurs at high temperatures, depending on the crystallization conditions of each material. Firstly, the MA is used to mix the initial powders. Following this, calcination is applied to form the crystallite phase, and the materials powders is compressed into bulk pellets. Finally, these bulk pellets are sintered to create ceramic pellets. An example of the solid-state reaction process is illustrated in Figure 15.

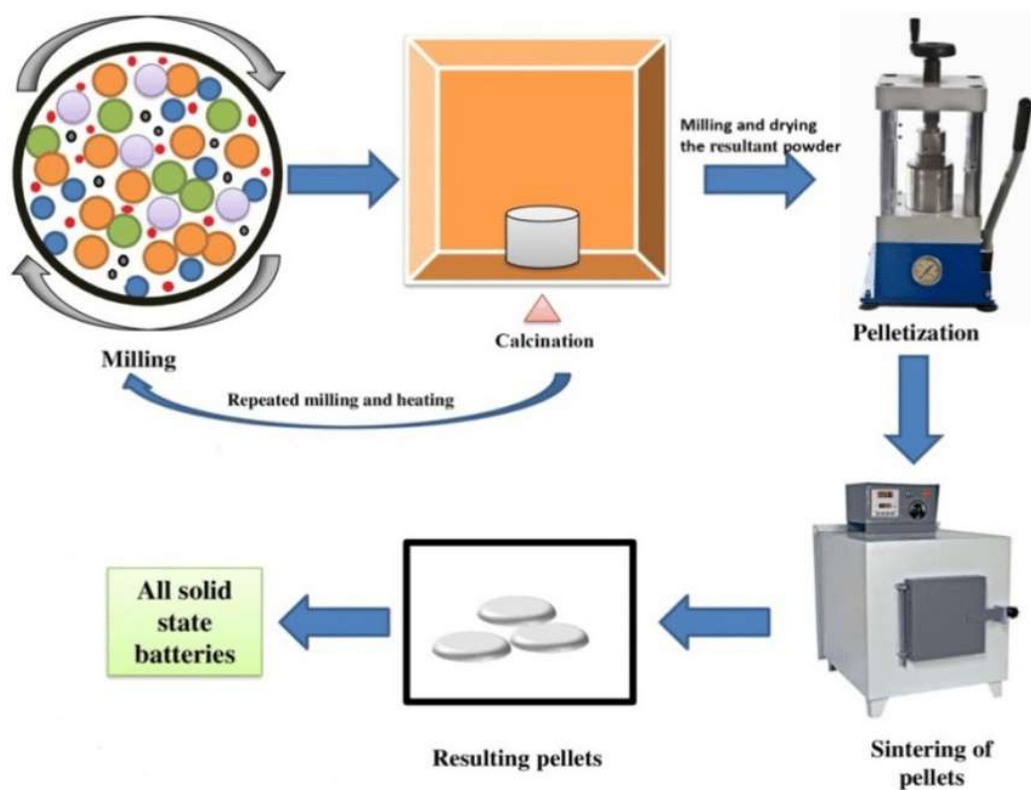


Figure 15 Schematic representation of solid-state reaction method (Sodhiya *et al.*, 2021).

2.2.3 Beta zinc antimonide β -Zn₄Sb₃

In the Zn–Sb system, the commonly studied crystalline phases include ZnSb, Zn₃Sb₂ and Zn₄Sb₃ (Adjadj *et al.*, 2006). The Zn₄Sb₃ which has polymorphs of α -Zn₄Sb₃, β -Zn₄Sb₃ and γ -Zn₄Sb₃, was investigated in terms of its phase diagram by Mayer K. W. in 1978 (Mayer *et al.*, 1978). Among these polymorphs, The β -Zn₄Sb₃ stands out as an excellent thermoelectric material, particularly in the intermediate temperature range of 200–400 °C (473.15–673.15 K), with a maximum figure of merit (ZT) of approximately 1.3 at 400 °C (Caillat *et al.*, 1997; Ur *et al.*, 2003). The crystalline structure of β -Zn₄Sb₃ is of the hexagonal rhombohedral space group $R\bar{3}c$. The structure of β -Zn₄Sb₃ contains 30 Sb atoms and 36 Zn atoms per a unit cell (Snyder *et al.*, 2004; Mayer *et al.*, 1978). Zn atoms are partially occupied at the positions 36 Zn(1) site(f) and interstitial positions 36 Zn(1, 2, 3, 4) site(e, f), with varying occupancy percentages (%). Similarly, Sb atoms are partially occupied at the positions 18 Sb(1) site(e) and 12 Sb(2) site(c), also with different occupancy percentages (%). The current issue is determining the accurate model for β -Zn₄Sb₃ among the proposed models of Zn₃₉Sb₃₀, Zn₆Sb₅ and Zn₁₃Sb₁₀ (Nylén *et al.*, 2004; Bokii and Klevtsova, 1965; Snyder *et*

al., 2004). Models for $\text{Zn}_{39}\text{Sb}_{30}$ and $\text{Zn}_{13}\text{Sb}_{10}$ are shown in Figure 16 while the Zn_6Sb_5 model is depicted in Figure 17.

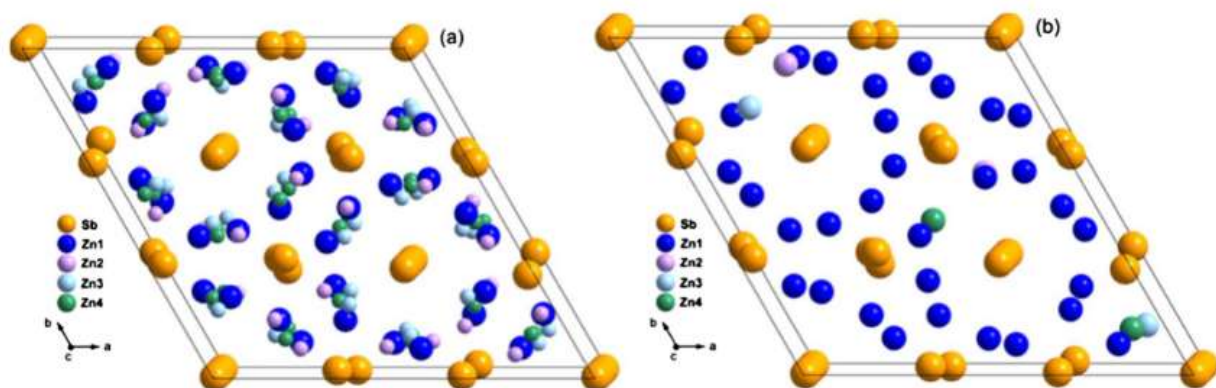


Figure 16 (a) Crystalline structure model of $\text{Zn}_{39}\text{Sb}_{30}$ and (b) Crystalline structure model of $\text{Zn}_{13}\text{Sb}_{10}$ (Zou *et al.*, 2015).

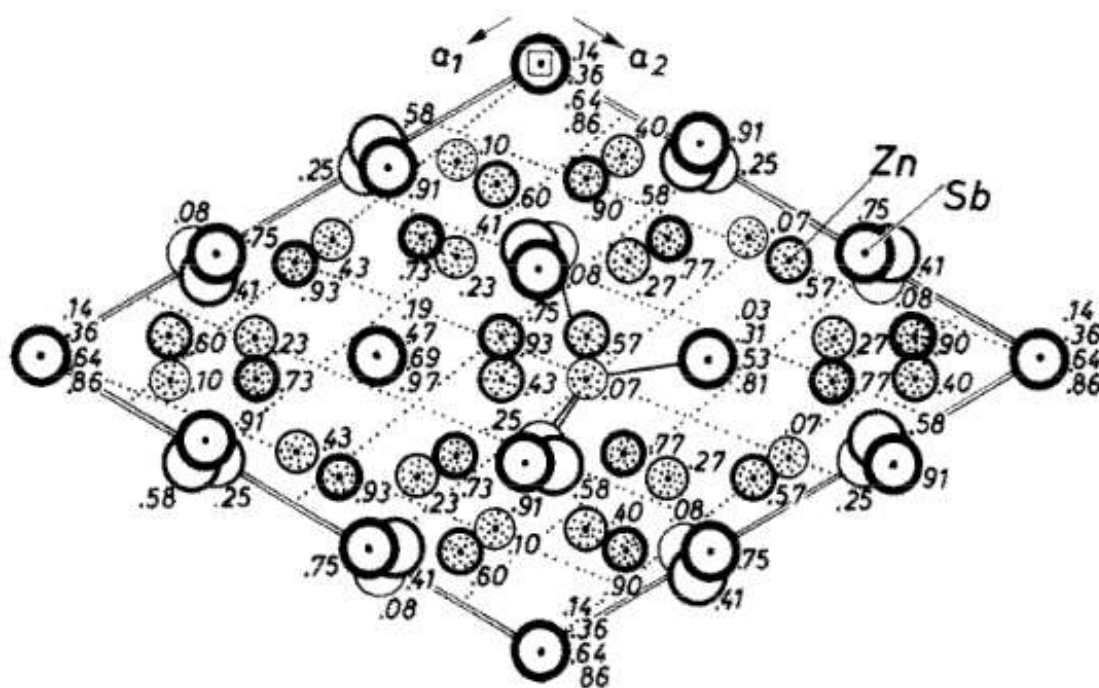


Figure 17 Crystalline structure model of Zn_6Sb_5 (Mayer *et al.*, 1978).

In the Zn_6Sb_5 model or Mayer model, Zn atoms occupy the position 36 Zn(1) site(f) at 100% and 18 Zn(1) site(e) at 11% while Sb atoms are positioned at the position 18 Sb(1) site(e) at 89% and 12 Sb(2) site(c) at 100% occupancy. In the $Zn_{39}Sb_{30}$ or three interstitial model, Zn atoms are found the position 36 Zn(1) site(f) at 90% occupancy, interstitial positions 36 Zn(2) site(f) with approximately 5%, and 36 Zn(3) site(f) with around 6% occupancy. Sb atoms are located at the position 18 Sb(1) site(e) and 12 Sb(2) site(c) at 100% occupancy each. The full occupancy model, closely matches the experimental X-ray diffraction results for β - Zn_4Sb_3 (Qiu *et al.*, 2010). In this model, Zn atoms occupy the positions 36 Zn(1) site(f) at 100% and have no occupancy at interstitial positions, while Sb atoms occupy the position 18 Sb(1) site(e) at 100% and 12 Sb(2) site(c) at 100%. A comparison of the structural models for β - Zn_4Sb_3 is presented in Table 3.

Table 3 Comparison of structure model β -Zn₄Sb₃ with intermediate step to interstitial model (Snyder *et al.*, 2004).

Site multiplicity	Site occupancy (fraction)			
	Zn(1) (36f)	Sb(1) (18e)	Sb(2) (12c)	Zn Interstitial (36f)
Mayer Model	1	0.89 Sb 0.11 Zn	0	1
Full occupancy Model	1	1	1	0
Three interstitial Model	0.9	1	1	0.17

The calculated X-ray diffraction pattern for the Zn₃₉Sb₃₀, Zn₆Sb₅ and Zn₁₃Sb₁₀ models appear very similar, with nearly identical diffraction peaks. This research, the synthesized β -Zn₄Sb₃ powders were compared with Mayer's model of Zn₆Sb₅ because of Mayer's model of Zn₆Sb₅ was refined based on calculations and experiment. The X-ray diffraction (XRD) patterns for the Zn₃₉Sb₃₀, Zn₆Sb₅ and Zn₁₃Sb₁₀ models are shown in Figure 18, Figure 19 and Figure 20, respectively.

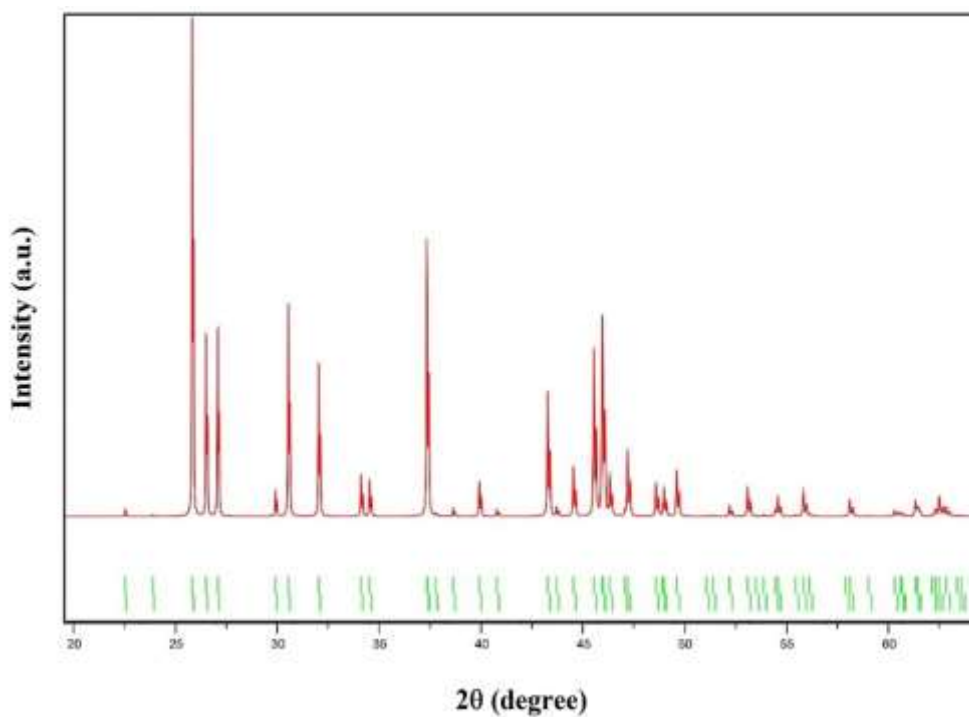


Figure 18 Calculated X-ray diffraction pattern yields of $Zn_{39}Sb_{30}$ model by using Boru's CIF- 7040405 (Borup *et al.*, 2016).

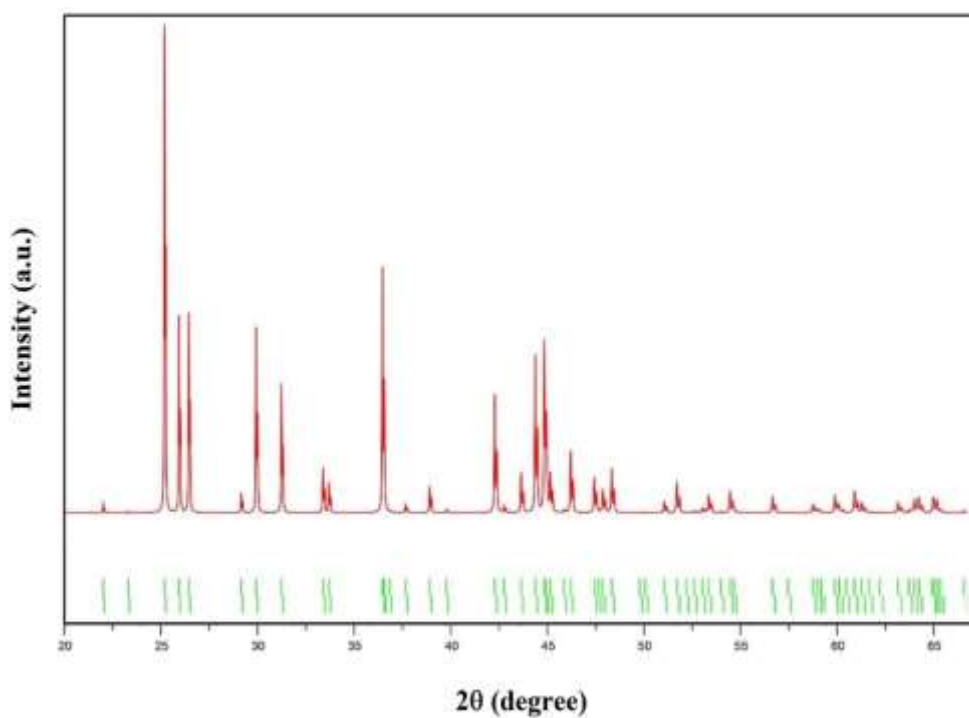


Figure 19 Calculated X-ray diffraction pattern yields of Zn_6Sb_5 model by using Jeffrey Snyder's CIF-cm0515505_si_001(Snyder *et al.*, 2004).

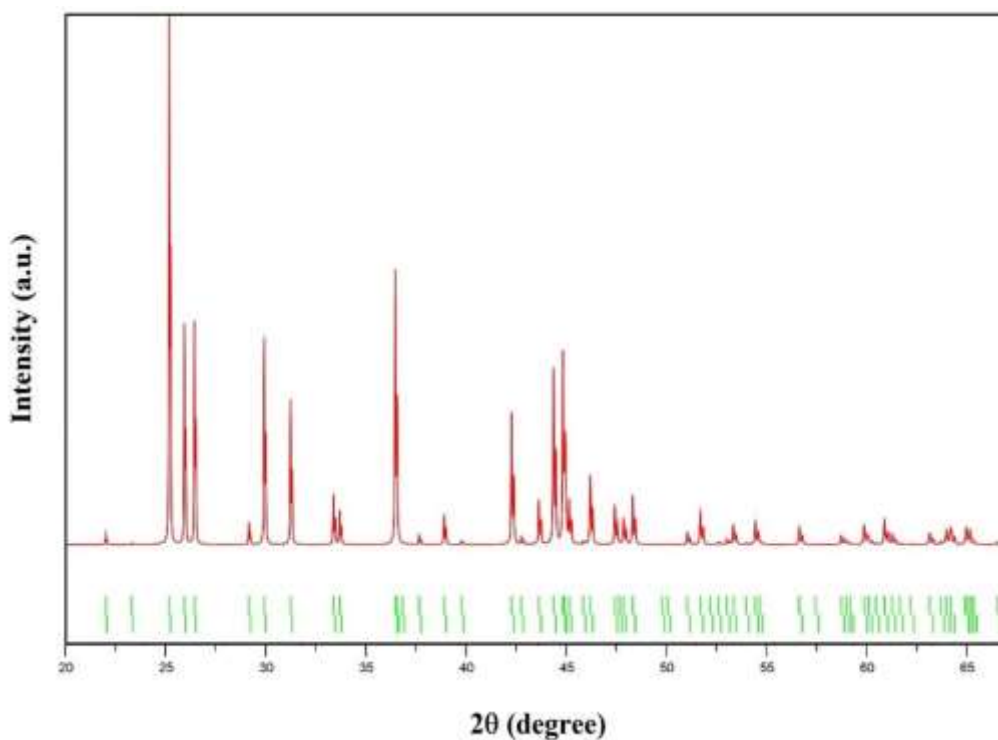


Figure 20 Calculated X-ray diffraction pattern yields of $\text{Zn}_{13}\text{Sb}_{10}$ model by using Yurij's CIF- 4001474 (Mozharivskij *et al.*, 2006).

The most popular method for synthesizing high-purity $\beta\text{-Zn}_4\text{Sb}_3$ materials is quenching. This process involves placing powdered Zn and Sb elements into a sealed quartz tube filled with argon gas, heating the mixture to 700–750°C to melt it into ingot of $\beta\text{-Zn}_4\text{Sb}_3$ (Lin *et al.*, 2014; Böttger *et al.*, 2011). The ingot is crushed into powder using a ceramic mortar and pestle. The XRD patterns of the $\beta\text{-Zn}_4\text{Sb}_3$ powders amply produced by both Lin and Böttger's research groups were found to match the calculated XRD patterns of the $\text{Zn}_{39}\text{Sb}_{30}$, Zn_6Sb_5 and $\text{Zn}_{13}\text{Sb}_{10}$ models. XRD pattern of quenched $\beta\text{-Zn}_4\text{Sb}_3$ materials are displayed in Figure 21 (Böttger *et al.*, 2011). Although, high pure $\beta\text{-Zn}_4\text{Sb}_3$ materials can be synthesized using the quenching method, it is not optimal for producing large quantities due to the challenges associated with filling the quartz tube with precursors and crushing the material into fine $\beta\text{-Zn}_4\text{Sb}_3$.

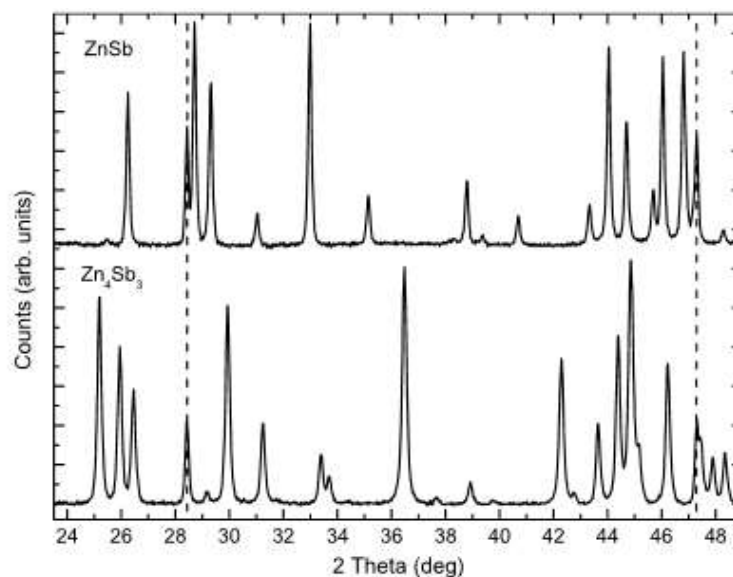


Figure 21 XRD yields of ZnSd (top) and Zn₄Sb₃ (bottom) were prepares by quenching method (Böttger *et al.*, 2011).

The Mechanical alloying method is also used to prepare β -Zn₄Sb₃, making it suitable for conventional production and large-scale synthesis (Lee and Lin, 2018). The β -Zn₄Sb₃ powders synthesized using this method exhibit an XRD pattern similar to those produced by the quenching method. The XRD pattern of the β - powders synthesized through mechanical alloying is shown in Figure 22. As well known, Zn element can evaporate at temperature of 350 °C. Therefore, when using the calcination method, it is important to compensate for this by adding extra Zn powder to the sample precursors to ensure optimal synthesis (Ueno *et al.*, 2006; Ito *et al.*, 2003; Shim *et al.*, 2015).

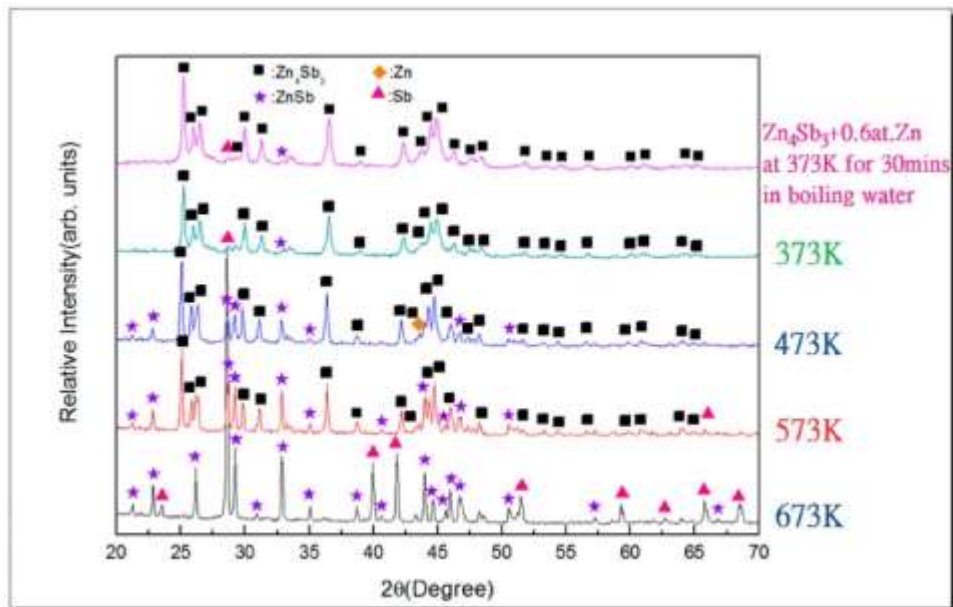


Figure 22 XRD pattern of β - Zn_4Sb_3 with 0.6 at. % Zn rich via different sintered temper- atures in vacuum (Lee and Lin, 2018).

The mechanical alloying (MA) method is a materials synthesis technique that uses a ball mill to grind and mix initial precursor elements, forming crystalline phase and homogeneous mixture. However, since the crystalline phase is often incomplete after milling, the precursors are further calcined and sintered to fully develop the crystalline structure, a process known as the "solid-state reaction method". This thesis employs the solid-state reaction process to synthesis β - Zn_4Sb_3 powders. According to the MA method, the precursor powders formed small crystalline phase of β - Zn_4Sb_3 , ZnSb , Sb and Zn phases as shown in the XRD results in Figure 23. SEM images of the precursor powders before and after using MA method are shown are Figure 24. Generally, the thermoelectric materials are typically pressed into ceramic pellets to study its thermoelectric properties and for use usage in modules. Therefore, the compression and sintering processes were studied to determine the optimal conditions for fabricating β - Zn_4Sb_3 ceramic with homogeneous surfaces and minimal porosity (Ahn *et al.*, 2011). The surfaces of the β - Zn_4Sb_3 ceramic pellet were influenced by temperature and pressure that presented in Figure 25 and Figure 26.

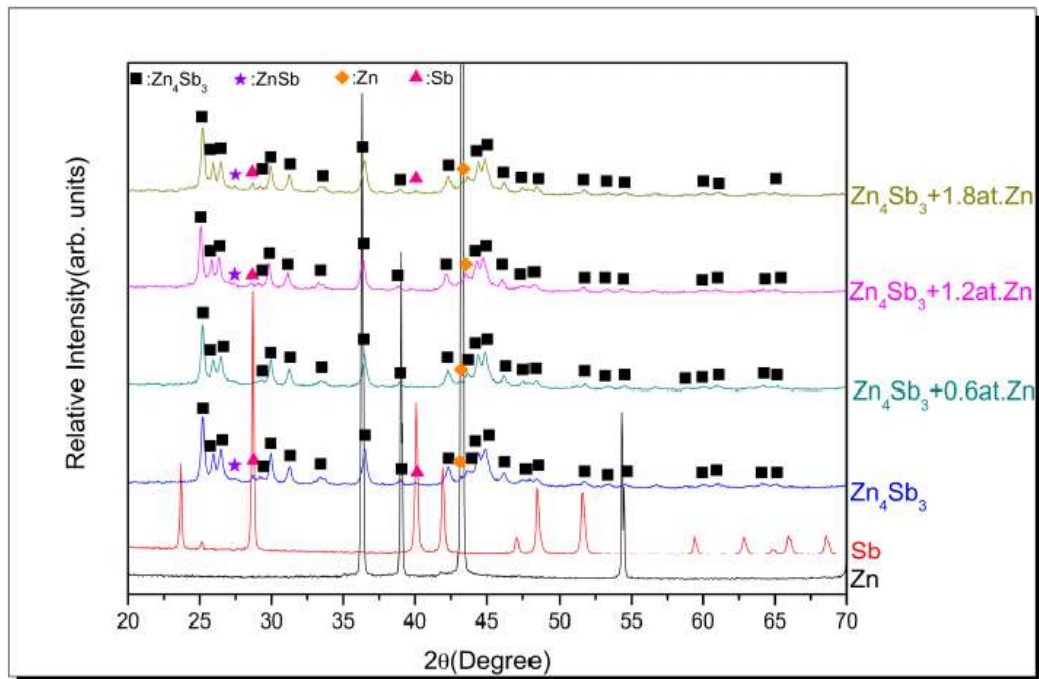


Figure 23 XRD pattern of milled $\beta\text{-Zn}_4\text{Sb}_3$ with different at. % Zn rich (Lee and Lin, 2018).

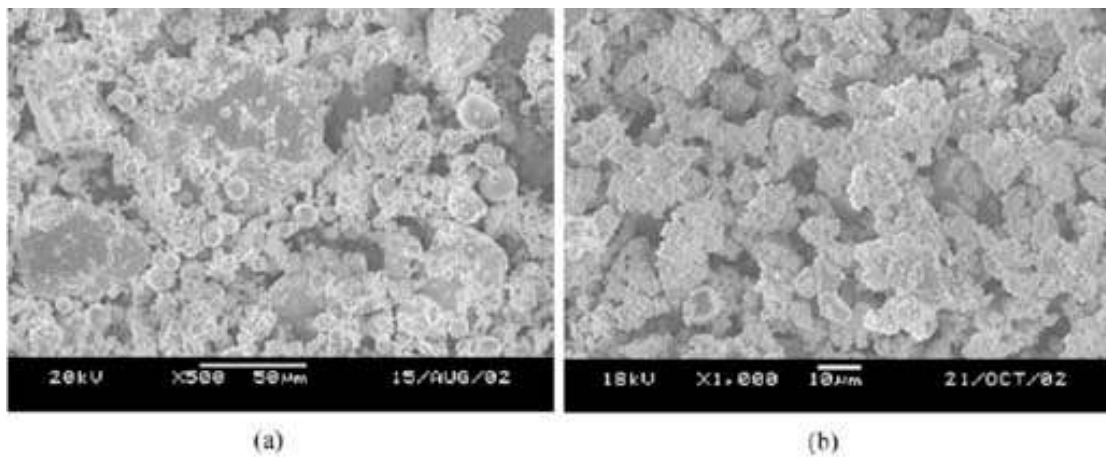


Figure 24 SEM images of $\beta\text{-Zn}_4\text{Sb}_3$ powder; (a) Before mechanical alloying method and (b) After mechanical alloying method (Ur *et al.*, 2003).

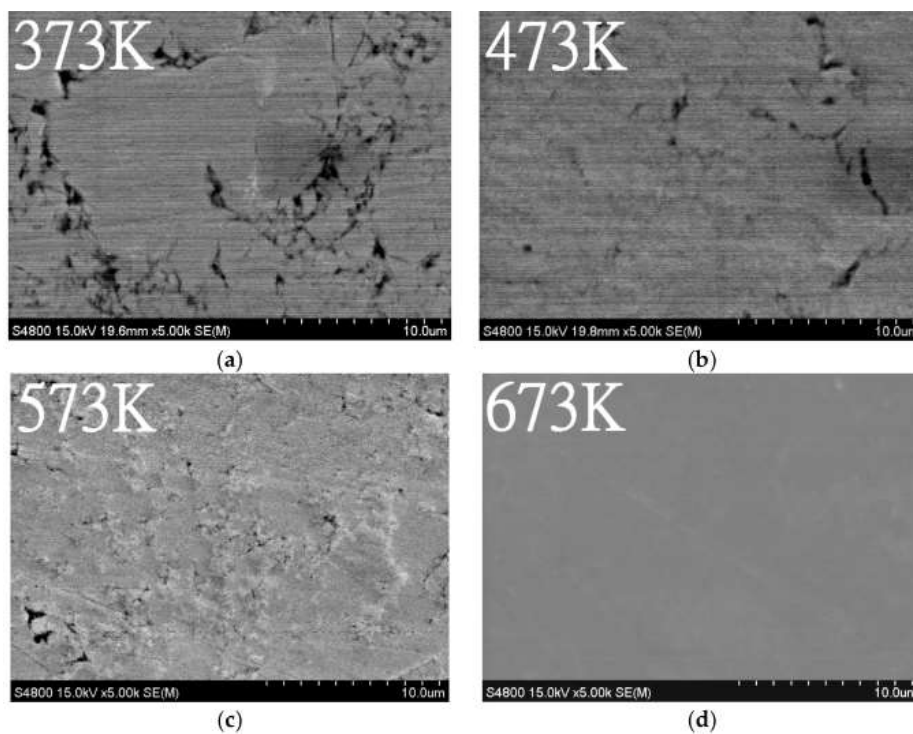


Figure 25 SEM images of hot-pressed β - Zn_4Sb_3 ceramic at temperatures of 373 K, 473 K, 573 K and 673 K with pressure 0.98 GPa (Lee and Lin, 2018).

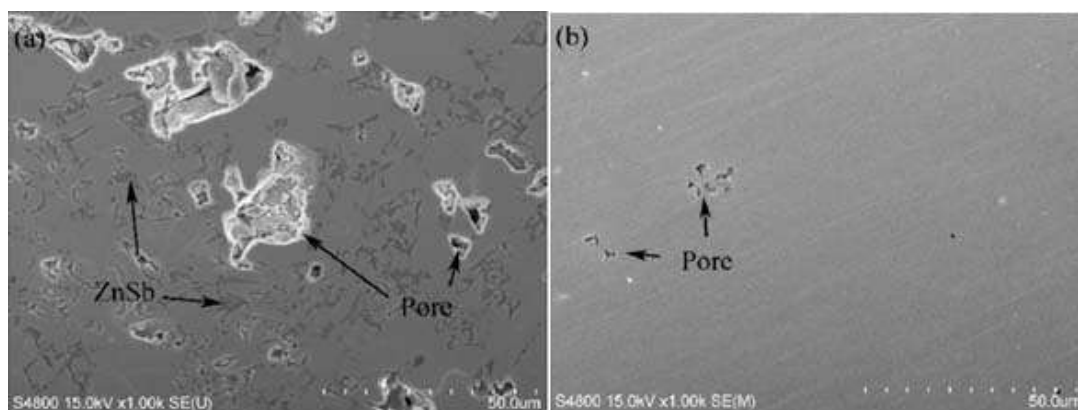


Figure 26 SEM images of hot-pressed β - Zn_4Sb_3 ceramic with pressing pressures of 100 MPa (a) and 200 MPa (b) at 673 K (Ahn *et al.*, 2011).

Based on the experimental results, applying high pressing pressure and sintering at elevated temperatures leads to reduced porosity and a smooth surface on β - Zn_4Sb_3 pellet ceramic. Additionally, these conditions result in higher density, which significantly affects the Seebeck coefficient, thermal conductivity, and electrical conductivity. According to the research by Ahn J.H. and colleagues, they observed that

applying a high pressure of 250 MPa during the compression of β -Zn₄Sb₃ ceramic pellets resulted in an improved Seebeck coefficient of 200 $\mu\text{V}/\text{K}$ at 673 K, stable thermal conductivity ranging from 0.7–0.6 W/mK at 473–673 K, and low electrical resistivity (indicating good electrical conductivity) of 115 $\mu\Omega\text{m}$ across the same temperature range (Ahn *et al.*, 2011). The effects of pressing pressure on the Seebeck coefficient, thermal conductivity, and electrical conductivity are illustrated in Figure 27. This thesis, high pressing pressure and elevated sintering temperatures were employed to fabricate β -Zn₄Sb₃ ceramic pellets.

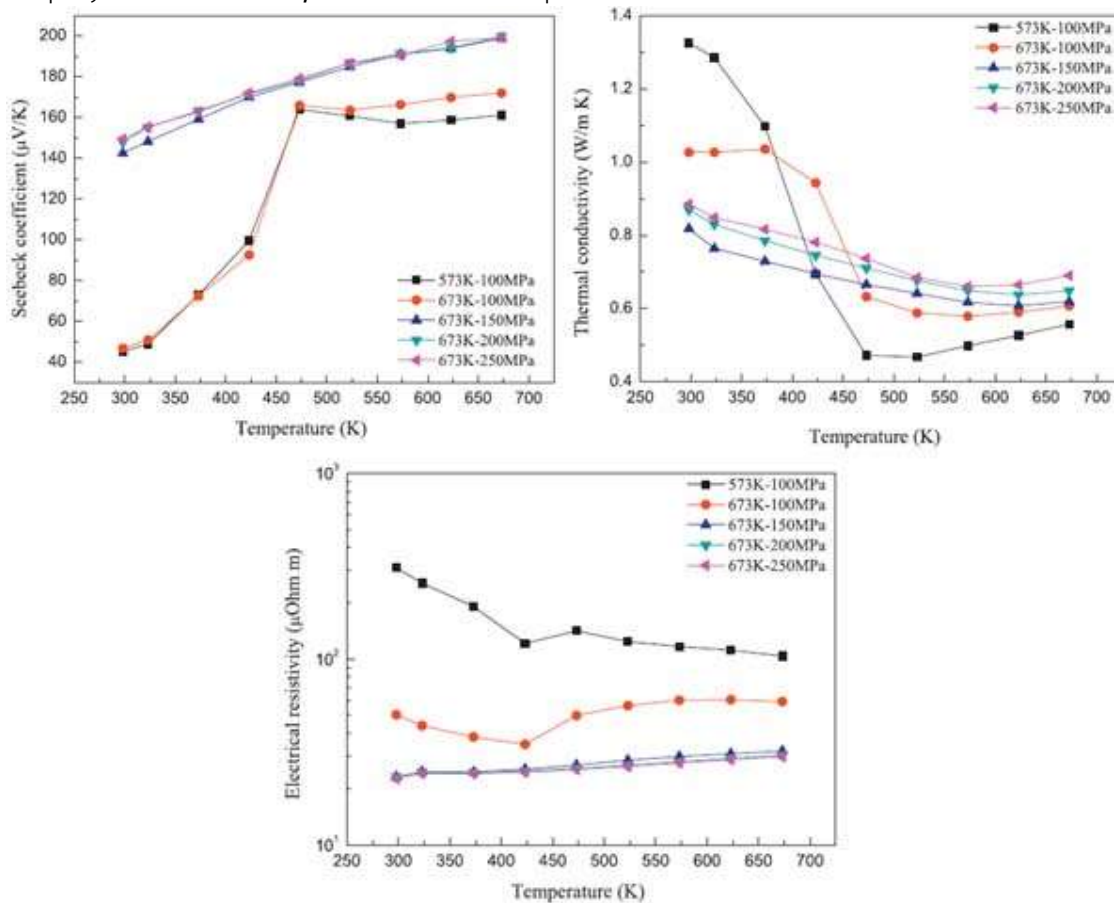


Figure 27 Seebeck coefficient, thermal conductivity and electrical conductivity of hot-pressed β -Zn₄Sb₃ ceramic pellets via different temperatures and pressure (Ahn *et al.*, 2011).

2.3 Thermoelectric generator modules

Thermoelectric generators modules are key components in electronic devices, used to directly convert heat into electrical current since the 19th century. The thermoelectric effect, first discovered by Thomas Johann Seebeck in 1821, Typically, thermoelectric generators (TEGs), also known as longitudinal TEGs, are constructed

using either dual-leg or single-leg designs. In the dual-leg TEGs, both P-type and N-type thermoelectric materials are used, with electric and heat transport occurring parallel to each other along isotropic properties (Crawford, 2014). In contrast, single-leg TEGs are made with either P-type or N-type thermoelectric materials, as shown in Figure 28 and Figure 29, respectively. On the other hand, transverse thermoelectric (TTE) modules, where the directions of electric and heat transport are perpendicular, are primarily used in applications like thermal radiation detectors, thermocouples, and cooling systems. The transverse thermoelectric modules often feature serpentine or tilted arrangements with anisotropic properties, as illustrated in Figure 30.

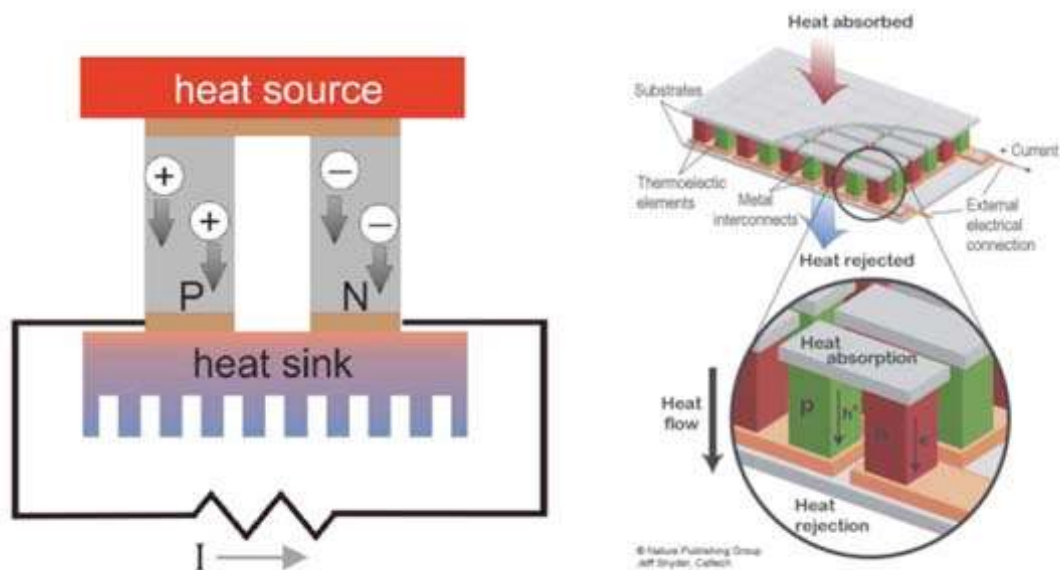


Figure 28 Schematic of a dual leg TEG module and dual leg series TEG device with isotropic properties (Crawford, 2014).

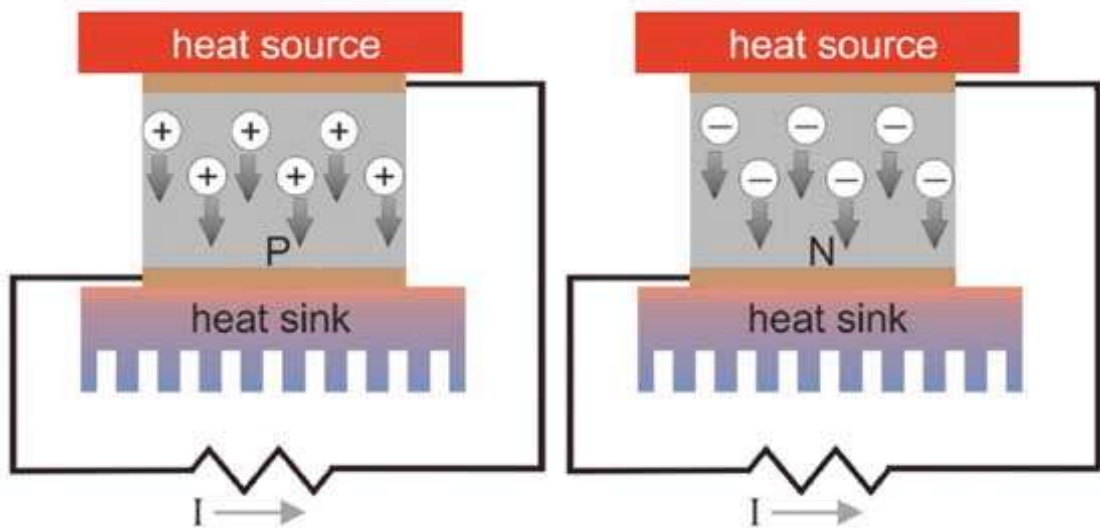


Figure 29 Schematic of single leg TEG module with isotropic properties (Crawford, 2014).

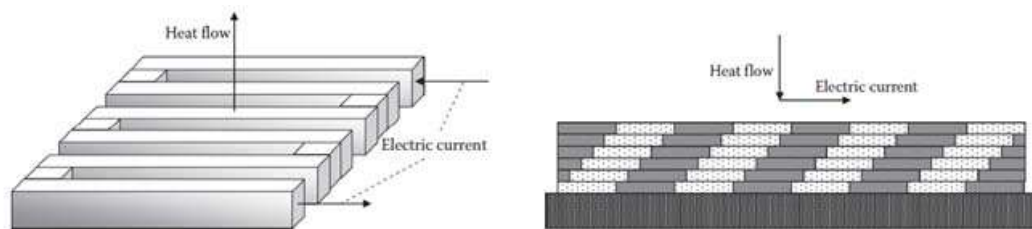


Figure 30 Schematic of serpentine and tilted-multilayer TTE module with anisotropic thermoelectric properties (Goldsmid, 2017).

TTE modules have gained popularity since the 19th century, with developments in tilted ceramic block TTE and artificially tilted TTE films (Zahner *et al.*, 1998; Kyarad and Lengfellner, 2006; Reitmaier *et al.*, 2010; Dreßler *et al.*, 2015; Kanno, 2016; Mu *et al.*, 2019; Li *et al.*, 2022; Uchida, 2022). Mostly, the studies have focused on improving the performance of TTE modules to make them suitable as TEG modules for powering microelectronic devices (Bathen and Linder, 2017; Jaworski *et al.*, 2010; Kim *et al.*, 2021; Uchida, 2022; Mu *et al.*, 2019). The TTE films module and TTE ceramic pellet module are shown in Figure 31 and Figure 32. However, TE modules have not yet matched the performance of TEG modules due to limitations such as electrical current loss and high electrical resistivity. These issues are primarily caused by the tilted angle of the TTE module, which leads to the formation of self-resistance barriers within the module (Goldsmid, 2017).

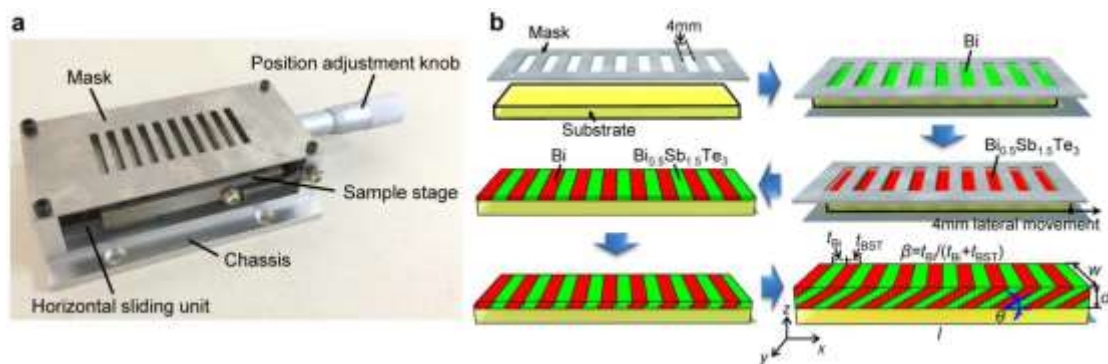


Figure 31 (a) Photograph of misaligned make assembly equipment for sputtering Bi/Bi_{0.5}Sb_{1.5}Te₃ TTE device, (b) Illustration of layer by layer stacking of Bi/Bi_{0.5}Sb_{1.5}Te₃ (Mu *et al.*, 2019).

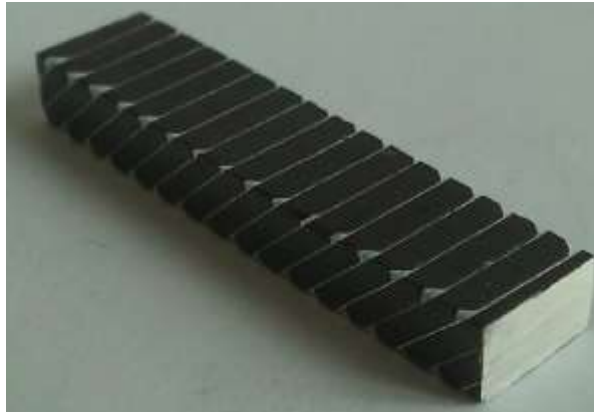


Figure 32 Tilted ceramic block TTE device prepared by $\text{La}_{1.97}\text{Sr}_{0.03}\text{CuO}_4$ with silver paste connector (Dreßler *et al.*, 2015).

Recently, a new TEG model known as the monolithic TEG module has been developed. This all-in-one TEG module features a structural design that simplifies fabrication processes. Various thermoelectric configurations can be applied to the monolithic TEG module, as shown in Figure 33. A key aspect of all monolithic TEG modules is the use of alternative resistive materials to separate TEG cells and conductive materials for electrical connections, such as ZO, SiO_2 , Ag, Ag_2S -alloy (Lai *et al.*, 2022). The terminal positions of electrical charges for different monolithic TEG module designs, such as single leg, dual leg, unileg, and transverse are illustrated in Figure 34. Huajun L. and his research team reported on the fabrication process of monolithic $\text{Ag}_2\text{S}_{0.2}\text{Se}_{0.8}/\text{Ag}_2\text{S}/\text{Bi}_{0.5}\text{Sb}_{1.5}\text{Te}_3$ TEG modules, which are dual-leg TEG models consisting of three alloy materials of $\text{Ag}_2\text{S}_{0.2}\text{Se}_{0.8}$, $\text{Bi}_{0.5}\text{Sb}_{1.5}\text{Te}_3$, Ag_2S as n-type, p-type and insulator materials, respectively (Lai *et al.*, 2022) (Dreßler *et al.*, 2015). However, this monolithic TEG module is limited to low-temperature applications due to the material constraints of $\text{Ag}_2\text{S}_{0.2}\text{Se}_{0.8}$ and $\text{Bi}_{0.5}\text{Sb}_{1.5}\text{Te}_3$ materials (Mansouri *et al.*, 2021; Singh *et al.*, 2020). The monolithic $\text{Ag}_2\text{S}_{0.2}\text{Se}_{0.8}/\text{Ag}_2\text{S}/\text{Bi}_{0.5}\text{Sb}_{1.5}\text{Te}_3$ TEG modules is shown in Figure 35.

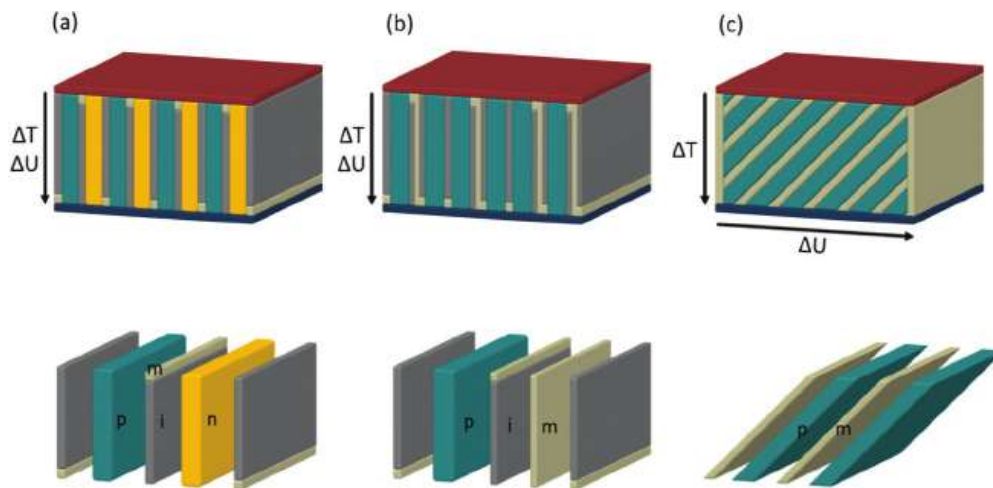


Figure 33 Schematic of dual leg, unileg and transverse series monolithic TEG device (Dreßler *et al.*, 2015).

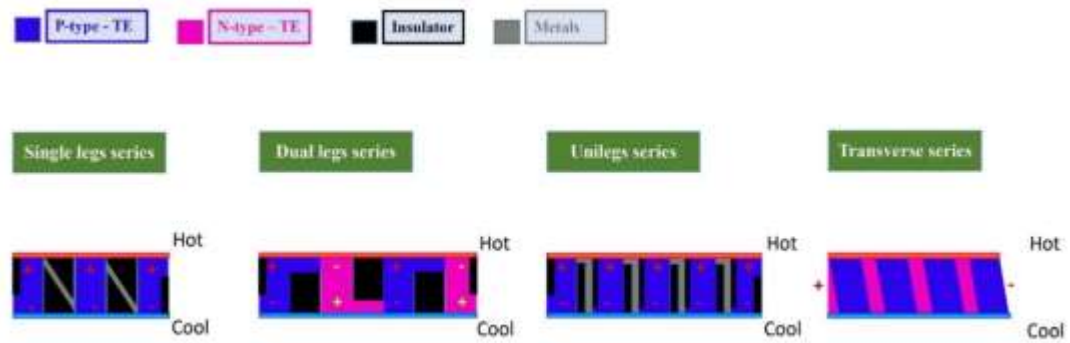


Figure 34 Illustration of charge positions of all monolithic TEGs model.

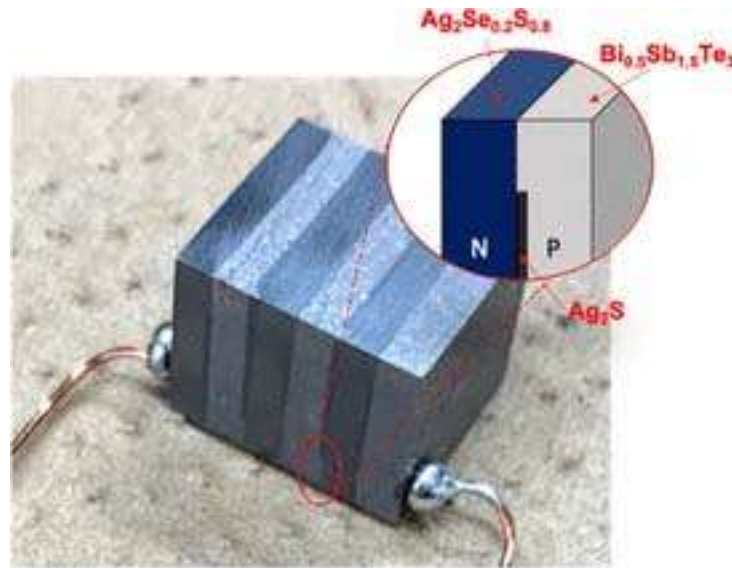


Figure 35 Monolithic $\text{Ag}_2\text{S}_{0.2}\text{Se}_{0.8}/ \text{Ag}_2\text{S} / \text{Bi}_{0.5}\text{Sb}_{1.5}\text{Te}_3$ TEG modules.

To simplify the fabrication processes of TEG modules and enhance for using in industrials waste heat recycling, in this thesis presents the development of novel single leg series monolithic $\beta\text{-Zn}_4\text{Sb}_3/\text{ZnO}$ TEG modules with a modified zigzag electrical connection. Synthesized $\beta\text{-Zn}_4\text{Sb}_3$ and commercial ZnO were used as p-type thermoelectric material and insulator material, respectively (Jantrasee *et al.*, 2016). The $\beta\text{-Zn}_4\text{Sb}_3$ powers were synthesized through solid-state reaction and calcination under a flow of Ar gas flow. These powders were characterized and used to prepare sintered $\beta\text{-Zn}_4\text{Sb}_3$ pellets, which thermoelectric properties were evaluated. Efficient performance of the monolithic $\beta\text{-Zn}_4\text{Sb}_3/\text{ZnO}$ TEG modules was assessed by measuring the electrical power output, calculated deploying equation of

$$P_{\text{out}} = NI^2R_L = N \left[\frac{S(T_h - T_c)}{R_g + R_L} \right]^2 R_L \quad (109) \quad (\text{Goldsmid, 2010}).$$